Precise nanofiltration in a fouling-resistant self-assembled membrane with water-continuous transport pathways

Xunda Feng[1,2,†], Qaboos Imran[2,3,†], Yizhou Zhang[3,†], Lucas Sixdenier [4], Xinglin Lu[2], Gilad Kaufman[2], Uri Gabinet[2,3], Kohsuke Kawabata[5], Menachem Elimelech[2], and Chinedum O. Osuji[2,3*]

[1] Center for Advanced Low-dimension Materials, State Key Laboratory for Modification of Chemical Fibers and Polymer Materials, Donghua University, Shanghai 201620, China

[2] Department of Chemical and Environmental Engineering, Yale University, New Haven, CT 06511, USA

[3] Department of Chemical and Biomolecular Engineering, University of Pennsylvania, Philadelphia PA 19104

[4] ESPCI Paris, 10 Rue Vauquelin, 75005 Paris, France

[5] Department of Chemistry, Graduate School of Science, Tohoku University, 6-3 Aoba, Aramaki, Aoba-Ku, Sendai, Japan

*Email: cosuji@seas.upenn.edu

† These authors contribute equally.

Abstract

Self-assembled materials are attractive for next-generation membranes as they circumvent the limitations of pathway tortuosity and size-dispersity of transport-regulating features found in conventional membranes. However the need to align self-assembled nanostructures such as cylinders and lamellae, and the narrow windows of stability for bicontinuous gyroid systems present challenges, as does preservation of mesophase structure during processing to form mechanically robust membrane materials. We propose and demonstrate a novel approach that relies on transport in a water continuous medium of a nanostructured polymer templated from a direct lyotropic H_1 mesophase. Composition optimization of a polymerizable cationic surfactant system enables retention of the hexagonally-ordered mesophase structure on photo-induced crosslinking. The high fidelity structure retention, confirmed by TEM and AFM imaging, and the mechanical robustness of the resulting material, rely on a dual-crosslinker strategy that results in a solid film consisting of internally and externally crosslinked nanofibrils embedded in a continuous aqueous medium. Fabricated membranes show strong size selectivity at the 1-2 nm length scale and high water permeabilities of ~ 10 L m^{-2} h^{-1} bar^{-1} μm. Moreover the membranes display excellent antimicrobial properties due to the presence of quaternary ammonium groups on the surfaces of the nanofibrils. The water-continuous nature combined with outstanding mechanical integrity and antimicrobial properties represent a breakthrough for polymerized lyotropic liquid crystal membranes and suggest these materials can serve in practical water purification applications.

Introduction

Membrane separations are widely used in existing technological applications including seawater desalination, gas separation, food processing and fuel cells, as well as in emerging areas, such as, sustainable power generation and distillation.(1) Nanofiltration (NF) involves the removal of dissolved or suspended solutes ranging from 1-10 nm in size. The development of new NF membranes is of particular interest for low-cost treatment of wastewaters to remove organic contaminants, including so-called contaminants of emerging concern such as pesticides and metabolites of pharmaceutical drugs.(2) Current state-of-the-art membranes, however, suffer from a generally recognized trade-off between permeability and selectivity: increasing permeability often results in decreased selectivity, and *vice versa*.(3, 4) This trade-off originates from the intrinsic structural limitation of these conventional membranes, i.e., a broad distribution of free volume elements in dense polymer membranes or pore sizes in porous membranes. Membranes based on self-assembled materials entail the use of nanostructures with near-monodisperse critical dimensions. Self-assembled materials have therefore been considered an attractive way to realize highly selective separations without compromising permeability.(5-7)

Block copolymers (BCPs) and small molecule liquid crystals (LCs) can self-assemble into a series of mesophase morphologies possessing periodic nanoscale domains with sizes and shapes that are thermodynamically defined. The well-ordered nanostructures found in BCPs and LCs, including cylinders,(8, 9) lamellae,(10) and gyroids, have been considered as attractive templates for the fabrication of nanoporous membranes.(8) Uniform-size nanopores may already exist intrinsically in some self-assembled systems, or they can be formed by selective removal of a

sacrificial component.(11-13) Membranes made by non-solvent induced phase separation of block copolymers represent a compelling advance in terms of selectivity (at the ~ 10 nm length scale) and scalability of fabrication.(14-17) Additionally, self-assembling materials provide useful templates for controlling the organization of discrete objects such as water channel proteins(*18*) or nanotubes(*19*), that can function as nanofiltration pores. While such nanoporous membranes have been demonstrated to show high selectivity and permeability for nanofiltration and ultrafiltration, challenges are still encountered in their practical development, as schematically outlined in **Figure 1A**.

For the readily accessed 1-D cylindrical and 2-D lamellar systems, the anisotropic nature of the nanostructures implies the need for uniform orientation throughout the system, e.g. vertical cylinders in a thin film, to produce an optimized morphology for membrane performance. Such optimized morphologies, however, do not spontaneously occur during membrane fabrication processes. Considerable efforts must be made to direct the self-assembly of nanostructured domains in thin films. To this end, previous studies have successfully employed interfacial engineering, e.g., top coating and surface anchoring,(*20-22*) or external fields such as magnetic fields.(*11*, *23*, *24*) Although these methods are reliable, they bring additional constraints that present significant, if not insurmountable, challenges for large-scale membrane fabrication. On the other hand, 3-D interconnected gyroid nanopores are advantageous over their cylindrical or lamellar counterparts, because the nanopores need no alignment to ensure continuity and optimized permeability in the resulting membrane.(*25-27*) However, access to gyroid morphologies is complicated by their generally narrow windows for phase stability in BCPs (*28*) and by the tailored molecular structures required in LC assemblies.(*29*, *30*) The aforementioned

challenges have combined to hamper the pursuit of high performance membranes derived from self-assembled materials. In addition to the need to optimize transport morphology, biofouling resistance is a significant concern. The generally poor biofouling resistance of current water treatment membranes and difficulties associated with their cleaning increase operating costs and are an important challenge to overcome.(*31*, *32*)

Here, we report a scalable approach to obtain highly permeable and selective nanofiltration membranes that also exhibit attractive anti-biofouling properties, specifically, antimicrobial activity. The membranes make novel use of a morphology consisting of hexagonally ordered molecular nanofibrils (**Figure 1B**). This morphology is realized by crosslinking a direct cylindrical (H_1) lyotropic LC (**Figure 1C**). In contrast to gyroid phases, the H_1 mesophase occurs more frequently and exhibits stability in a much wider composition window in lyotropic systems. While the H_I phase obviates the need for alignment, care must be taken in the formulation of the system to ensure the ability to crosslink in place, without loss of structure. The membranes described here are based on mesophases that have been optimized for high fidelity retention of the structure of the lyotropic precursor in the crosslinked system. The membrane is mechanically robust and is resilient against both dehydration and swelling by excess water. We surmise that these properties originate due to structural cohesion provided by topological defects present in the system and water-bridging crosslinks between cylindrical structures. The notion that a polymerized direct lyotropic system would retain its structure in aqueous media is counter-intuitive, and represents a strong departure from prior reported work.(*33*) The self-assembled structure provides a uniform and well-defined spacing between nanofibrils, thereby leading to high membrane selectivity. More importantly, the availability of a three-dimensionally

continuous transport path in the membrane obviates any need for structural alignment, thereby significantly reducing the complexity of membrane fabrication. These characteristics definitively set the currently reported membranes apart from nanostructured membranes derived from lyotropic liquid crystals reported to date, and offer a path towards viability in practical nanofiltration operations.

Figure 1. Schematic illustration of self-assembled structures used to fabricate nanoporous polymer membranes. (A) The two readily obtained morphologies, i.e., lamellae and cylinders, require alignment of the structures to optimize transport. (A) Schematic illustration showing self-assembled morphologies utilized as templates for fabricating nanoporous polymer membranes. Two easily obtained morphologies, i.e., lamellae and cylinders, while used for forming nanopores, require alignment of the self-assembled domains. 3-D interconnected gyroids are not universally observed in BCP and LC systems, and where they occur, usually exhibit narrow windows of stability. (B) The proposed morphology for fabricating membranes that can be easily templated from mesophases of hexagonally packed cylinders and requires no alignment to enhance flux. (C) Schematic illustration for preparation of size exclusion nanofiltration membranes from crosslinking of a direct hexagonal cylinder lyotropic mesophase (H_1). The crosslinked sample contains hexagonally packed molecular fibrils in the continuous water phase, which allows water to permeate through the gap between nanofibers but rejects larger-size solutes due to size exclusion. (D) Molecular structures of the polymerizable surfactant 2-(methacryloyloxy)ethyl tetradecyl dimethyl ammonium bromide (METDAB), the water soluble crosslinker oligo(ethylene glycol) dimethacrylates (OEG-DMA) and the oily crosslinker ethylene glycol dimethacrylate (EG-DMA) for the formulation of the desired H_1 mesophase. ED-GMA (in green) copolymerizes with the surfactant in the hydrophobic core and water soluble OEG-DMA (in blue) bridges each cylinder into a network, the morphology of which provides a continuous aqueous transport path, as schematically illustrated.

Results and discussion

A cationic surfactant, 2-(methacryloyloxy)ethyl tetradecyl dimethyl ammonium bromide (METDAB), bearing a polymerizable methacrylate group close to the hydrophilic head, was utilized to formulate a polymerizable H_1 mesophase with water and additional crosslinkers, ethylene glycol dimethacrylate (EG-DMA) and oligo(ethylene glycol) dimethacrylate (OEG-DMA) (**Figure 1D**). The surfactant monomer, or surfmer, was synthesized in a single step Menshutkin reaction(*34*), details of which can be found in the **Materials and Methods**. The METDAB/water binary phase diagram at room temperature displays isotropic micellar solution (L_1), hexagonal cylindrical phase (H_1), bicontinuous gyroid phase (G), and lamellar phase (L_α), as the surfactant concentration is increased from 0 to 100 wt.% (**Supplementary Materials, Figure S1**). The formation of H_1 phases at room temperature occurs in a range of METDAB concentration from roughly 55 to 80 wt.%.

One approach to obtain an ordered polymerized nanofibril structure is by photo-initiated polymerization of H_1 mesophases.(*35*) For membrane applications, it is of critical importance to achieve high-fidelity replication of the ordered nanostructures from the LC template. Previous studies have suggested the utilization of crosslinking to retain LC order, by introducing multiple polymerizable groups to the reactive amphiphiles(*25*, *30*) or by adding crosslinkers into the systems.(*10*, *20*, *36*, *37*) For the polymerization of H_1 mesophases formed by reactive surfactants bearing single polymerizable groups, hydrophobic crosslinkers that segregate into the micellar cores have been commonly employed.(*36*, *37*) While success has been claimed in some cases, prior studies on polymerization of H_1 systems have typically relied on qualitative interpretations

provided by 1-D X-ray diffraction data and low-resolution polarized optical microscopy (POM) images for structural characterization. Missing in these efforts has been high resolution real-space imaging, for example by transmission electron microscopy (TEM) or atomic force microscopy (AFM), of the nanostructures produced after crosslinking. Such real-space imaging along with higher resolution POM characterization are vitally important for assessing the fidelity of structure retention after crosslinking. X-ray scattering data alone is unfortunately often less sensitive than required. It is therefore unclear to what extent structural preservation is achieved in the reported systems. Here, we performed detailed structural characterizations using a combination of high resolution small-angle X-ray scattering (SAXS) with high resolution microscopy (high resolution POM and direct imaging by TEM and AFM) to verify the retention of our formulated H_1 mesophase after UV-initiated crosslinking.

Results of crosslinking experiments carried out on H_1 mesophases that are not optimally formulated highlight the points made above regarding structure retention and appropriate characterization thereof. Photo-initiated polymerization of H_1 mesophases simply formed by METDAB/water binary systems in a broad range of compositions resulted in significant disruption of the H_1 morphology, as evidenced by the apparent cloudiness developed in the polymerized samples, the indiscernible LC textures in POM images and the shift of the SAXS peak ratio from 1: $\sqrt{3}$ to 1: $\sqrt{4}$ (**Supplementary Materials, Figure S2**). Although the presence of an added crosslinker may improve the structural retention of the system on polymerization, disruption still occurs. While the disruption is not easily recognized at first by X-ray scattering due to the preservation of the 1: $\sqrt{3}$ SAXS peak ratios, and POM, it is seen in the subtle changes to the LC texture of developable domains in high resolution POM images and the tendency to

form lamellar structures observed in TEM images that may explain the unexpected increase of the (200) peak intensity after polymerization found in both the system here and a previous study (**Figure S3**).(*37*) Our observations mirror the polymerization-induced phase transformation or phase-separation observed in lyotropic mesophases.(*38*)

We employed a dual crosslinking strategy to more robustly preserve the H_1 morphology and to thereby circumvent the structural disruption issue described above: EG-DMA is insoluble in water, and therefore presumably sequesters selectively within the hydrophobic cores of the cylindrical micelles of METDAB. Addition of EG-DMA is therefore expected to help crosslink the interior of the cylindrical micelles into nanofibrils. Conversely, we pursued the addition of a hydrophilic counterpart, OEG-DMA, with the express intention that it bridge the aqueous spaces between the crosslinked nanofibrils to form a tight network (**Figure 1D**). In this perspective, OEG-DMA serves not only to improve morphology retention during polymerization, but also to provide mechanical integrity in the resulting polymer films which must be robust enough to permit pressure driven permeation in use as membranes. An optimized composition of 70 wt.% METDAB, 22.8 wt.% water, 5.4 wt.% OEG-DMA, and 1.8 wt.% EG-DMA was developed that formed a stable, homogeneous H_1 mesophase gel (**Figure 2A**). The EG-DMA was itself mixed with a small amount of a photo-initiator 2-methoxy-2-phenylacetophenone (10 wt.%) to facilitate photo-induced crosslinking of the mesophase. The photo-initiator concentration in the system overall was therefore 0.18 wt.%.

Figure 2. High-fidelity retention of the H_1 mesophase morphology after UV-induced crosslinking with the aid of dual crosslinkers. (A) Photo of an H_1 mesophase gel formed by 70 wt.% METDAB, 22.8 wt.% water, 5.4 wt.% OEG-DMA, and 1.8 wt.% EG-DMA. (B) Photos showing the corresponding crosslinked polymer film (40 μm thick) and the film integrity after immersion in water for 24 h. (C) 1-D integrated SAXS data displays the structural consistency of the H_1 morphology in the non-crosslinked gel, the crosslinked polymer, and the polymer after immersion in water for 24 h. A small increase of the d_{100} spacing from 3.6 to 3.7 nm was found after 24 h of water immersion, indicating that there was very little swelling of the sample. (D) POM image displaying the preservation of the typical LC texture found in cylindrical mesophases. (E) Schematic illustration of the shear alignment and the 2-D SAXS measurements. 2-D SAXS patterns before and after crosslinking as obtained by incidence of the X-ray beam (F) parallel and (G) orthogonal to the shear direction. (H) POM images showing the essentially unchanged birefringent color of the oriented cylindrical micelles before and after crosslinking. The sample was positioned such that the original shear direction was at 45° with respect to each of the two crossed polarizers. TEM micrographs viewed along (I) and orthogonal to (J) the shear direction showing aligned nanofibrils. Insets: fast Fourier transform images. Prior to microtoming, the polymer was immersed into a 0.1 wt.% KI aqueous solution for 1 h to replace Br^- by I^- to enhance the atomic number contrast for imaging. Photo credit: Xunda Feng, Yale University.

Phase transformation and phase separation on UV-induced crosslinking were successfully suppressed for the optimal gel composition as reflected by the excellent transparency of a representative resulting sample (**Figure 2B**). Moreover, the observed physical integrity on handling and the preservation of high optical transparency of the film after immersion in water for 24 h indicates that the system is resistant against structural collapse due to water swelling. Such retention of structural integrity is a critical necessity for a working membrane that remains in contact with aqueous streams for extended durations. Rheological measurements indicate that the shear modulus of cross-linked H_1 films is approximately 0.1 GPa, highlighting the mechanical integrity of the materials.

SAXS data provides more reliable information on the structural retention after crosslinking and subsequent water swelling (**Figure 2C**). The unchanged ratio of scattering peak locations (1: $\sqrt{3}$: $\sqrt{4}$) as shown in the 1-D integrated data demonstrates the intact hexagonal morphology after crosslinking. The d_{100} spacing of 3.6 nm was the same before and after UV-exposure, highlighting the fact that there was no change of lattice parameter during crosslinking. The primary Bragg peak width became marginally broader after crosslinking, with an increase of 0.018 nm^{-1} in the full width at half maximum (**Supplementary Materials, Figure S4**), suggesting a slight reduction in structural correlation length after polymerization. As for the polymer immersed in water for 24 h, we observed negligible swelling of the network, evidenced by a small (~ 2%) increase of the d_{100} spacing from 3.6 to 3.7 nm. These findings demonstrate the effectiveness of our dual crosslinker strategy for retaining structural order post-crosslinking and producing a mechanically resilient nanostructured film with water continuous domains. Time-dependent SAXS measurements on the influence of the d_{100} spacing by water swelling

suggest that the ~2% lattice parameter change occurred within 30 min (**Supplementary Materials, Figure S4**). In addition, the structural robustness of the crosslinked film after swelling is further reflected in the maintenance of the developable domain LC texture shown in the POM image (**Figure 2D**). Furthermore, larger-area and higher-resolution views in POM images also display no optical inhomogeneity within the LC domains (**Supplementary Materials, Figure S4**).

The retention of the original H_1 structure in the crosslinked polymer is also apparent by comparing SAXS data of a shear-aligned specimen before and after UV-exposure. **Figure 2E** shows the schematic illustration of the shear induced alignment and the incident directions of the X-ray on the sample. 2-D SAXS images as obtained by incidence of the X-ray beam along and orthogonal to the shear direction display patterns with 6-fold and 2-fold symmetries, respectively, which can be preserved in the corresponding crosslinked polymer (**Figure 2F, G**). The unperturbed orientations of both cylindrical axes and hexagonal lattices strongly demonstrate that the H_1 morphology was effectively locked in by crosslinking. As expected, POM images further show the same birefringent color of the sheared aligned sample before and after crosslinking (**Figure 2H**).

A high resolution TEM image, as shown **Figure 2I**, was obtained for an approximately 150 nm thick section microtomed perpendicular to the shear direction (**Supplementary Materials, Figure S5**). The polymer sample before sectioning was stained by immersing into a 0.1 wt.% KI aqueous solution to enhance atomic number contrast. An ordered array of hexagonally packed nanofibrils can be observed, with the inset FFT pattern displaying 6-fold symmetry. The cores of

the nanofibrils shown in the TEM are brighter than the matrix due to the reduced electron transparency of the fibril outer wall as stained by iodine ions. A d_{100}-spacing of 3.6 nm was calculated from the FFT pattern of this TEM image, in good agreement with the SAXS data. TEM visualization orthogonal to the shear direction (**Figure 2J**) displays the orientation of the nanofibrils along the shear direction, and the corresponding FFT image with 2-fold symmetry. To the best of our knowledge, this is the first TEM data that shows the successful production of ordered nanofibril arrays from polymerization or crosslinking of lyotropic H_1 mesophases. On the basis of the structural characterization data, we anticipate controlling dimensions of ~1.1 nm and ~0.5 nm for transport parallel, and perpendicular to the nanofibrils, respectively (**Supplemental Material, Figure S6**).

Figure 3. Fabrication of H_1/PAN composite membranes and microscopic characterization of the membrane structures. (A) Schematic illustrating H_1 membrane fabrication on supporting PAN membranes. (B) Photograph of H_1/PAN composite membrane. (C) Cross-sectional SEM image showing the composite membrane. (D) AFM images showing the surface morphology of the H_1 membrane with closely-packed nanofibrils. Topological defects including dislocations, disclinations and grain boundaries are well-preserved on the film surface, consistent with high-fidelity retention of the mesophase morphology on crosslinking. (E) Line-profile analysis of the high-resolution image (scale bar 20 nm) shows an inter-fibril distance of ~ 4 nm, in good agreement with SAXS and TEM measurements. Sinusoidal fit of the line profile provides a guide to the eye. Photo credit: Xunda Feng, Yale University.

The water-continuous nature, mechanical resilience and ordered self-assembled morphology of the crosslinked H_1 mesophase are attractive for membrane applications. The ability of the system to function as a membrane was assessed in a proof-of-concept manner. Membranes were produced by crosslinking a thin film of the H_1 mesophase spread on commercially sourced polyacrylonitrile (PAN) ultrafiltration membranes (Sterlitech, with molecular weight cut-off of ~400 kDa) that were used as mechanical supports. As schematically illustrated in **Figure 3A**, the process involves spreading of the H_1 gel onto a PAN support, followed by a mechanical pressing step to produce a thin gel film, and subsequent UV exposure for crosslinking (detailed procedures in the **Materials and Methods**). The resulting crosslinked H_1 film was contiguous with the supporting PAN membrane, as shown in the photo of the H_1/PAN composite membrane (**Figure 3B**) and the SEM image of the cross-sectional view (**Figure 3C**). The continuity of structure (i.e. absence of delamination) suggests there is appreciable adhesion between the film and the PAN. In fact, the mesophase typically penetrated some distance (~ 10s of microns) into the PAN support during pressing (**Supplementary Material, Figure S7**). While such penetration could be useful in avoiding delamination, it lends uncertainty in the determination of the effective thickness of the H_I film. In terms of the well-identified layer above the PAN surface, the procedure resulted in H_1 films with thickness in the range of approximately 3 to 30 μm as visualized by SEM.

The surface morphology of the H_1 membrane was characterized by AFM. Planarly oriented arrays of nanofibrils connected by typical topological defects including grain boundaries, dislocations, and disclinations can be clearly observed in the high-resolution AFM images (**Figure 3D**). An inter-fibril spacing of approximately 4 nm was obtained from the cross-

sectional analysis of an AFM image (**Figure 3E**). The morphology of randomly oriented nanofibril domains may contribute to the membrane's structural integrity because of the effective entanglement provided by topological defects connecting domains of different orientation. However, given the structural stability observed on extended swelling studies as well as on drying, the role of the OEG-DMA in covalently crosslinking nanofibrils is expected to be equally, if not more, important.

Solute rejection experiments were assessed by challenging the H_1 composite membrane with solutions containing a series of charged (cationic) and neutral molecules, with geometric mean sizes (diameters) ranging from 0.6 to 3.1 nm in a pressurized stirred cell (detailed in **Supplementary Materials, Figure S8**). Anionic dyes were not utilized to avoid the potentially confounding role of molecular fouling due to adsorption onto the positively charged nanofibril exterior. Experiments were conducted over extended periods (several hours to several days) to ensure that the results were representative of steady-state performance, rather than reflecting any transient effects due to dead-space in the filtration cell, solute adsorption, membrane compaction, or any inadvertent leaching of material from the system (**Supplementary Material, Figure S9**). The results of single-solute rejection experiments are summarized in **Figure 4A**. The solute sizes are geometric mean sizes determined from molecular dimensions calculated using the Chem3D software package. The supporting PAN membrane data is given as the control. The composite membrane displays strong size selectivity towards charged organic dye molecules, demonstrating rejection of ~90% or higher for methylene blue (AB, ~320 Da), crystal violet (CV, ~408 Da) and alcian blue 8G (AB, ~1300 Da). Complete AB rejection by the H_1 membrane is visible from the colors of the feed solution, and the permeate from the H_1 membrane, respectively: the blue

color from AB effectively disappears from the permeate (**Figure 4B**). Meanwhile, the lower solute rejection of the PAN support by itself indicates that the selectivity of the composite membrane is dominated by the H_1 layer. The H_1 membrane did not reject $CoCl_2$, suggesting that the effective pore size in the system is larger than the limiting 0.8 nm diameter of hydrated Co^{2+} ions. The molecular weight cut-off (MWCO) and size cut-off for the charged solutes were ~ 350 Da and 1 nm, respectively. The membranes were also selective against neutral solutes, but with a shift in the cut-offs to ~ 4 kDa and ~ 2.5 nm. The H_1 composite membrane completely rejects lysozyme (~14.3 kDa) at the isoelectric point, while both cobalamin ($VB_{12,}$ ~ 1400 Da) and riboflavin (VB_2, ~ 380 Da) are only moderately rejected.

The transport data indicate that the membranes can separate solutes effectively based on size as well as charge. Competitive rejection tests involving filtration of solutions containing 2 solutes were performed, for solutes of different size, and different charge, respectively. In the former case, a mixture of $CoCl_2$ and CV was fully separated, with complete rejection of CV, and zero rejection of Co^{2+} (**Figure 4C**). For the latter case, the membrane was challenged with a mixture of CV and VB_2. Analysis of the permeate shows that CV was completely rejected by the membrane, while the VB_2 was approximately 50% rejected (**Supplementary Materials, Figure S10**).

The rejection data highlight the important role of electrostatic interactions, i.e. Donnan exclusion, in the transport properties of these membranes. At the same time, relative to the theoretical transport dimensions of the mesophase (**Supplementary Material, Section S1**), and under the assumption that diffusion through the nanofibrils (rather than flow around them) is prohibited,

the rejection data for neutral solutes suggests that transport may be compromised by the presence of defects of some sort. It is possible that such defects originate due to imperfections associated with the mechanical pressing or another step in the membrane fabrication process. Another possibility is that topological defects in the mesophase provide less restrictive paths for solute transport. It is likely that continued refinement of the membrane fabrication process, and specifically, a departure from mechanical pressing methods, will improve the selectivity of the membranes by reducing defects such as those described here. It is worthwhile noting however that the assumption of zero permeability through the nanofibrils has not been rigorously tested here. While we expect that diffusion of water-soluble dyes through the hydrophobic nanofibrils would represent a very high resistance pathway, in the limit of sub-nm scale interstitial spaces, it represents the only transport pathway for solutes. Additional investigation along these lines may be fruitful, particularly in terms of highlighting the boundary between porous and solution diffusion mechanisms in polymer membranes.

The thickness-normalized pure water permeability of the H_1 membranes was determined to be ~10 L m^{-2} h^{-1} bar^{-1} μm, using free-standing membranes to avoid the uncertainty in thickness due to PAN penetration. Water permeability decreased by up to 50% during filtration of charged solutes, but was unaltered in the presence of neutral solutes. The high water fluxes observed for the system are consistent with the presence of a physically continuous transport path. Notably, the water permeability is considerably higher than that reported for membranes templated from gyroid LCs.(*25*) It is anticipated that a high water flux well above 100 L m^{-2} h^{-1} bar^{-1} can be realized when the thickness of the H_1 film is reduced to the range of 200 nm. These permeabilities, current and anticipated, compare favorably to those of commercial nanofiltration

membranes, such as Dow Filmtec NF90-400 that have permeabilities of roughly 10-15 L m^{-2} h^{-1} bar^{-1}.

Figure 4. Solute rejection and antibacterial properties of H_1 membranes. (A) Rejection data of H_1 membranes and PAN membranes for seven different solutes: Co (II), MB, CV, AB, VB2, VB12 and lysozyme. Spacing filling models and estimated geometric mean diameters of the solutes are shown. Error bars represent 95% t-test confidence limits derived from data variance across multiple measurements, typically 2 membranes and 4 permeate samples per membrane. (B) Photos of the feed solution of AB, the permeate from the H_1 membrane, and DI water as a reference, respectively. (C) UV-Vis spectrum and photo showing competitive solute separation of CV and Co (II). (D) Quantification of bacterial growth in colony forming units (CFU) in the samples and photographs (insets) showing control and H_1-derived membrane samples after incubation with bacteria. Photo credit: Yizhou Zhang, University of Pennsylvania and Xinglin Lu, Yale University.

The presence of the water-facing quaternary ammonium groups on the nanofibrils due to the surfactant self-assembly suggests that the membranes may exhibit anti-biofouling behavior, due to the well-established antimicrobial properties of these functional groups.(*39*, *40*) The potential for anti-biofouling behavior of H_1 membranes was studied using a standard colony-forming unit (CFU) enumeration assay(*41*, *42*) (details in the Supplementary Materials). Bare PAN membranes were also investigated as a control for comparison. In a typical experiment, a PAN or an H_1 membrane was kept in contact with a model Gram negative bacterium (*Escherichia coli*) in suspension for 3 h. The membranes were mildly sonicated in saline solution to detach bacteria from their surfaces that were subsequently cultured on Agar and incubated overnight. Photos in **Figure 4D** show the Agar plates of *E. coli* colonies cultured from cells on the control and the H_1 membrane. The CFU data shows that the number of viable *E. coli* cells from the H_1 membrane was 3 orders of magnitude smaller than that of the control. The strong reduction in CFU for H_1 membranes is consistent with a strong antimicrobial response, as anticipated due to the presence of the quaternary ammonium groups. It is worth noting however that biofouling due to bacterial growth is only one aspect of the complex problem of membrane biofouling, and fouling overall.

Conclusion

In conclusion, we have reported here a facile approach to fabrication of polymer nanofiltration membranes with a unique morphology of ordered arrays of nanofibrils. The approach utilizes a crosslinkable, water-continuous lyotropic H_1 mesophase as a template to realize the desired morphology. Our formulation of the H_1 mesophase takes the advantage of dual crosslinkers to preserve the ordered nanostructures with high fidelity and ensure mechanical robustness of the

resulting membrane. Systematic structural characterizations using POM, SAXS, high resolution AFM and TEM unambiguously confirm the formation of highly ordered nanofibrils in the crosslinked polymer membranes. Moreover, the direct imaging by TEM and AFM represents, to the best of our knowledge, the first such characterization of a polymerized lyotropic H_1 mesophase. The main constituent species of the system, METDAB, can be synthesized in large quantities in a single-step using readily available and inexpensive reagents. Production of large area, highly permeable and molecularly selective membranes for nanofiltration involves simple photo-induced crosslinking of the mesophase without any alignment procedure.

The membranes exhibit clear size-based selectivity when challenged with molecular dyes as model solutes and demonstrate thickness-normalized water permeabilities of ~10 L m^{-2} h^{-1} bar^{-1} μm. This high water flux is linked to the water-continuous structure templated from the water-continuous lyotropic liquid crystal. The disparity in the molecular weight cut-off for passage of neutral solutes relative to the theoretical limiting dimensions of the mesophase suggests defects are present. A reduction of such defects, for example by improvements in fabrication processes, can improve membrane selectivity. In the limit of very small interstitial spaces and low defect densities, these membranes may enable an assessment of the crossover from porous transport to solution diffusion.

We anticipate that additional improvements can be obtained by optimizing fabrication procedures to provide thinner selective layers, as well as through modification of the surface chemistry of the nanofibrils by the use of co-surfactants or post-functionalization to tune the cut-off characteristics of the membrane. Finally, the derived membranes demonstrate excellent

antimicrobial activity due to the intrinsic presence of quaternary ammonium groups. Such antimicrobial is beneficial in in mitigating biofouling, which is a pressing concern in practical membrane applications.

Materials and Methods

Materials

All chemicals used in this study were purchased from Sigma-Aldrich and used as received unless otherwise noted. The water soluble cross-linker oligo(ethylene glycol) dimethacrylate (OEG-DMA) has an average Mn of 750 as specified by the supplier. A radical photoinitiator 2-methoxy-2-phenylacetophenone was dissolved into the oil soluble cross-linker ethylene glycol dimethacrylate (EG-DMA) at a concentration of 10 wt.%.

Synthesis of Polymerizable Surfactant METDAB

Polymerizable surfactant 2-(methacryloyloxy)ethyl tetradecyl dimethyl ammonium bromide (METDAB) was synthesized by one-step Menshutkin reaction using a slightly varied procedure as reported in the literature.(*34*) 2-(Dimethylamino)ethyl methacrylate (31.4 g, 0.2 mol), 1-bromotetradecane (55.4 g, 0.2 mol), and anhydrous acetone (100 g) were mixed in a round-bottom flask. The mixture was stirred and heated at 45 °C in an oil bath for 48 h. After the reaction, the product, a white solid was precipitated from the solution by adding an excess amount of diethyl ether to the flask and then filtered using a Büchner funnel. The crude product was purified by recrystallization in ethyl acetate. The final product was rinsed several times by diethyl ether and filtered, followed by drying in vacuum for 12 h before use. The yield was above 70%.

Formulation of Lyotropic Liquid Crystals and Cross-linking

Lyotropic liquid crystals (LCs) can be formed by simply mixing the polymerizable surfactant METDAB and water. In order to preserve the mesophase morphologies, additional cross-linkers may be introduced into the system. The binary surfactant/water phase diagram was obtained by

systematic variation of the weight ratio of surfactant to water and characterization of the corresponding surfactant/water mixtures using POM and X-ray scattering. The formation of direct hexagonal phases (H_1) at room temperature was found to locate in the window of METDAB contents from 55 to 80 wt%. The cross-linkable H_1 phase utilized for the preparation of H_1 polymer membranes was obtained by mixing 70 wt% METDAB, 22.8 wt% water, 5.4 wt% OEG-DMA, and 1.8 wt% EG-DMA (doped with a radical initiator). This formulation was able to be cross-linked and give the excellent preservation of the H_1 morphology. Cross-linking/polymerization of mesophases was conducted in an N_2 atmosphere using a focused spot UV beam for 30 min (100 W Sunspot SM spot curing system at a distance of ~2 cm).

Polarizing Optical Microscopy (POM)

POM studies on LC textures were performed using a Zeiss Axiovert 200 M inverted microscope. LC samples sandwiched by two glass slides were slightly heated to facilitate the formation of the typical LC texture before POM visualization.

X-ray Scattering

2-D X-ray scattering data of mesophases before and after cross-linking were obtained using a Rigaku SMAX-3000 instrument with the accessible scattering vector (q) ranging from 0.015 to 0.24 $Å^{-1}$. The wavelength of the X-ray beam was 1.542 Å (Cu Kα radiation). X-ray scattering with higher q values were performed using a Rigaku 007 HF+ instrument with a rotating anode Cu Kα X-ray source and a 2-D Saturn 994+ CCD detector. The calibrations of the X-ray scattering instruments were done by using a silver behenate standard and a silicon powder standard, respectively. All the 2-D scattering patterns were integrated into 1-D plots of scattering intensity (I) versus q, where $q = 4\pi \sin(\theta)/\lambda$ and the scattering angle is 2θ.

Transmission Electron Microscopy (TEM)

The preparation of TEM samples is illustrated by **Figure S5**. Cross-linked H_1 samples were immersed into a 0.1 wt% KI aqueous solution for 1 h to enhance atomic number contrast. The stained sample was rinsed by water and completely dried before sectioning. The stained, cross-linked samples were then embedded into an epoxy specified for microtoming. The epoxy resin was cured at 50 ℃ for 12 h to ensure the required rigidity for sectioning. Samples were microtomed at room temperature by a diamond knife mounted on a Leica EM UC7 ultramicrotome. The thickness of the sections was set to 150 nm by the microtoming instrument. Sectioned samples were then transferred to a TEM grid and characterized by an FEI Tecnai Osiris TEM with an accelerating voltage of 200 kV.

Atomic Force Microscopy (AFM)

AFM studies on the surface morphology of the H_1 membranes were performed using the tapping mode of a Bruker Dimension Fastscan AFM instrument.

Rheological Characterization

Mechanical characterization of the crosslinked H_1 material was performed on an ARES G2 rheometer (TA Instruments) in the dynamic mode to determine the shear modulus of the system, using a 8 mm parallel plate with a gap height ~ 2mm.

Scanning Electron Microscopy (SEM)

SEM imaging on cross-sections of the H_1 membranes on supports was conducted by a Hitachi SU-70 instrument with an accelerating voltage of 5 kV.

UV-Vis Spectroscopy

UV-Vis spectra were recorded in transmission mode using a dual beam configuration on a Cary 300 spectrometer. Dye rejection was quantified by UV-Vis spectrophotometry of permeate solutions (diluted as necessary) compared with UV-Vis absorbances of calibrated dye standard solutions at the characteristic peak absorbance wavelengths of the solutes.

Fabrication of H_1/PAN membranes

Polyacrylonitrile (PAN) ultrafiltration membranes with a rejection size of 400 kDa were obtained from Sterlitech Corporation and the item No. was specified as YMPX3001 - Synder Flat Sheet Membrane. PAN membranes were employed in this study as mechanical supports for the H_1 active membranes. The procedure for the membrane fabrication is briefly illustrated by Figure 3a. Homogenized H_1 gel contained in a centrifugal tube was centrifuged at a speed of 14×10^3 rpm for 40 min to completely eliminate bubbles trapped in the gel before use. The degassed H_1 gel (~5-10 mg) was quickly placed on top of a smooth Mylar film (slightly stretched to ensure smoothness), followed by covering by a PAN membrane with the active PAN layer facing the H_1 gel. The Mylar/H_1/PAN construct was then sandwiched by two glass plates. Appropriate pressure was applied on the sandwiched construct for 5 min to ensure spreading of the gel on the PAN support. After that the glass plates were removed and the gel covered by the Mylar film was exposed to a focused spot UV beam for 10 min (100 W Sunspot SM spot curing system at a distance of ~2.5 cm) in an N_2 atmosphere. The Mylar film was then carefully peeled off from the cross-linked H_1 membrane.

Filtration Testing, Static Adsorption and Relevant Example Calculations

The hydraulic permeability and dye rejection quantification procedures were identical for the H_1/PAN membranes and the control PAN support. Roughly square coupons (approx. 2 cm × 2 cm) were installed into a 50 mL EMD Millipore Amicon (UFSC05001) stirred cell atop of a 4.5-cm diameter piece of polyester macroporous support (Sterlitech). The surface of the membrane was then covered with a customized circular stainless-steel mesh. The setup is shown in Figure S8 (Supplementary materials). Within the filtration cell, the active testing area of the membrane coupon was a circular area with a diameter of 1.1 cm, corresponding to an effective surface area of 0.95 cm^2. After loading the feed solution into the test cell chamber, compressed nitrogen gas was used to pressurize the test cell to pressures ranging from 0.5 to 80 psi. Permeate was collected in glass vials sealed with parafilm to prevent solvent evaporation.

During the rejection experiments, a constant pressure of 80 psi was maintained, and the cell was stirred at 400 rpm to reduce the concentration polarization. At least 1 mL of permeate was collected for each solute rejection experiment. After completion of tests with one dye and before testing the coupon with the next dye, the stirred cells and the membranes were rinsed with DI water thoroughly, followed by filtering at least 3 mL DI water through the coupon to rinse any residual solutes. To prepare the feed solution for single solute rejection experiments, Alcian blue 8G (AB), crystal violet (CV), methylene blue (MB), vitamin B12 (VB12) and lysozyme at a concentration of 0.5 g L^{-1} were dissolved in DI water. The solution pH for lysozyme solution was adjusted by dissolving the NaOH pellets within until the isoelectric point at pH = 11.35 was achieved, as monitored by using an Accumet AB15 pH meter (Fisher Scientific) coupled with pH test strips. Meanwhile, riboflavin (VB2) was dissolved in DI water at a concentration of 0.05 g L^{-1}. In the salt rejection experiment, $CoCl_2$ was dissolved in DI water at a concentration of 100 mM. To prepare the feed solution for competitive solute rejection experiments, mixture of

solutes was dissolved in DI water. Specifically, the VB2 and CV solution was prepared with an equal solute concentration of 0.05 g L^{-1}, and the $CoCl_2$ and CV solution was prepared at a concentration of 100 mM and 0.5 g L^{-1}, respectively.

The free-standing H_1 thin-films used for static solute adsorption experiment were prepared in a similar manner as the H_1 PAN composite, with minor modifications. Specifically, glass slides with sacrificial polymeric coatings were employed to sandwich the film during pressing. Two microscope slides (Fisher Scientific, pre-cleaned) were spin-coated (2000 rpm, 1 min) with aqueous polymer solutions, the first slide with 1 wt.% Dextran (M_n ~ 70 kg mol^{-1}) and the second slide with 1 wt% Chitosan (medium molecular weight) solutions, and were subsequently baked in a convection oven at 85 °C for 2 h. Measured amounts of H_1 gel (~10 mg) were sandwiched between a chitosan-coated slide and a dextran-coated slide. Upon the completion of photo-initiated cross-linking, the glass slide sandwiched H_1 thin film was plunged in a DI water bath for few hours until the dextran coating was fully dissolved to allow removal of the top slide. Following this, the H1 gel adhered to the bottom chitosan-coated slide was immersed in a 3 wt% acetic acid bath for 24 h, causing the dissolution of the chitosan coating and leading to a free-standing floating crosslinked thin-film of the H_1 gel. Subsequently, pieces of free-standing thin-films were then immersed in targeted solute solutions for 48 h with a packing ratio of ~0.2 g membrane per L solution. In the end, the concentrations of the solutions with H_1 free-standing thin-films were analyzed and compared with the reference stock solutions.

The hydraulic permeability was quantified by measuring the amount of time required to collect a certain volume into the collection vial. The following formula was used:

$$J = \frac{(m_{vial,final} - m_{vial,init}) \times (1/\rho)}{A \times (t_{final} - t_{final}) \times P} = \left[\frac{\mathrm{L}}{\mathrm{m^2 \cdot hr \cdot bar}}\right]$$

where,

m = mass of vial (in grams)
ρ = density of water (in grams/liter)
A = active membrane testing area (in square meters)
t = time (in hours)
P = gauge pressure (in bar)

A sample calculation is shown below for water permeability of an H_1 membrane:

$$A = \frac{\pi D^2}{4} = \frac{\pi[1.1 \times 10^{-2}\mathrm{m}]^2}{4} = 9.5 \times 10^{-5}\mathrm{m^2}$$

$$P = 80\ \mathrm{psi} \times \frac{1\ \mathrm{bar}}{14.5\ \mathrm{psi}} = 5.5\ \mathrm{bar}$$

$$J = \frac{(1.75) \times (1/1000)}{(9.5 \times 10^{-5}) \times (29) \times (5.5)} = 0.12\ \mathrm{L\ m^{-2} h^{-1} bar^{-1}}$$

UV-Vis spectrophotometry was used for concentration determinations to quantify dye rejection/selectivity performance of the tested membranes. The concentration of the permeate was determined from the linear regression plot from a series of standard concentrations. The dye rejection metric was calculated from UV-Vis spectra as shown here:

$$\%\ \mathrm{Rejection} = 100\% \times \left(1 - \frac{c_{permeate}}{c_{feed}}\right)$$

where,

$c_{standard}$ = concentration of standard dye solution (as weight fraction in DI water)
c_{feed} = concentration of feed dye solution (as weight fraction in DI water)

Colony Forming Units (CFU) Enumeration Assay

Escherichia coli (ATCC BW26437) were received from the Yale *E. coli* Genetic Stock Center. Bacteria were grown overnight in Luria-Bertani (LB) broth at 37 °C. After incubation, the culture was diluted in a fresh medium and grown until log phase (~1.5 h), as evidenced by an optical density of ~0.8 at 600 nm. The bacterial cells were washed three times with sterile saline solutions (0.9 wt.% NaCl) before use. CFU enumeration assay was used to evaluate the antimicrobial activity of the H_1 membranes. The bacterial suspension (10^8 CFU·mL^{-1}) was exposed to the membrane surface for 3 h at room temperature. After discarding the excess bacterial suspension, a 5-mL saline solution was used to rinse unattached cells from the film. The film was then transferred into another 5-mL saline solution and sonicated for 10 min in an ultrasonic bath (26 W·L^{-1}, FS60 Ultrasonic Cleaner) to detach bacteria from the film surface. After detachment of cells from the membrane surface, the supernatant was immediately cultured on an LB agar media and incubated overnight at 37 °C for CFU enumeration. Bare PAN membranes were also investigated as controls for comparison. Three independent samples were exposed to *E. coli* and the average value with one standard derivation was reported. All results were presented as means ± standard deviation. Statistical differences ($p < 0.05$) between two groups were determined using Student's *t* test with paired two-tailed distribution.

References

1. B. E. Logan, M. Elimelech, Membrane-based processes for sustainable power generation using water. *Nature* **488**, 313 (2012).
2. B. Du, A. E. Price, W. C. Scott, L. A. Kristofco, A. J. Ramirez, C. K. Chambliss, J. C. Yelderman, B. W. Brooks, Comparison of contaminants of emerging concern removal, discharge, and water quality hazards among centralized and on-site wastewater treatment system effluents receiving common wastewater influent. *Sci. Total Environ.* **466-467**, 976-984 (2014).
3. H. B. Park, J. Kamcev, L. M. Robeson, M. Elimelech, B. D. Freeman, Maximizing the right stuff: The trade-off between membrane permeability and selectivity. *Science* **356**, (2017).
4. D. L. Gin, R. D. Noble, Designing the Next Generation of Chemical Separation Membranes. *Science* **332**, 674-676 (2011).
5. Y. Zhang, J. L. Sargent, B. W. Boudouris, W. A. Phillip, Nanoporous membranes generated from self-assembled block polymer precursors: Quo Vadis? *J. Appl. Polym. Sci.* **132**, (2014).
6. J. R. Werber, C. O. Osuji, M. Elimelech, Materials for next-generation desalination and water purification membranes. *Nat. Rev. Mater.* **1**, 16018 (2016).
7. I. Sadeghi, P. Kaner, A. Asatekin, Controlling and Expanding the Selectivity of Filtration Membranes. *Chem. Mater.* **30**, 7328-7354 (2018).
8. M. J. Zhou, T. J. Kidd, R. D. Noble, D. L. Gin, Supported lyotropic liquid-crystal polymer membranes: Promising materials for molecular-size-selective aqueous nanofiltration. *Adv. Mater.* **17**, 1850 (2005).
9. W. A. Phillip, B. O'Neill, M. Rodwogin, M. A. Hillmyer, E. L. Cussler, Self-Assembled Block Copolymer Thin Films as Water Filtration Membranes. *ACS Appl. Mater. Interfaces* **2**, 847-853 (2010).
10. H. P. C. v. Kuringen, G. M. Eikelboom, I. K. Shishmanova, D. J. Broer, A. P. H. J. Schenning, Responsive Nanoporous Smectic Liquid Crystal Polymer Networks as Efficient and Selective Adsorbents. *Adv. Funct. Mater.* **24**, 5045-5051 (2014).
11. X. Feng, K. Kawabata, G. Kaufman, M. Elimelech, C. O. Osuji, Highly Selective Vertically Aligned Nanopores in Sustainably Derived Polymer Membranes by Molecular Templating. *ACS Nano* **11**, 3911-3921 (2017).
12. G. M. Bögels, J. A. M. Lugger, O. J. G. M. Goor, R. P. Sijbesma, Size‐Selective Binding of Sodium and Potassium Ions in Nanoporous Thin Films of Polymerized Liquid Crystals. *Adv. Funct. Mater.* **26**, 8023-8030 (2016).
13. T. Kato, From Nanostructured Liquid Crystals to Polymer-Based Electrolytes. *Angew. Chem. Int. Ed.* **49**, 7847-7848 (2010).
14. V. Abetz, Isoporous Block Copolymer Membranes. *Macromolecular Rapid Communications* **36**, 10-22 (2015).
15. P. Madhavan, K.-V. Peinemann, S. P. Nunes, Complexation-Tailored Morphology of Asymmetric Block Copolymer Membranes. *ACS Appl. Mater. Interfaces* **5**, 7152-7159 (2013).
16. S. P. Nunes, Block Copolymer Membranes for Aqueous Solution Applications. *Macromolecules* **49**, 2905-2916 (2016).
17. Y. Gu, U. Wiesner, Tailoring Pore Size of Graded Mesoporous Block Copolymer Membranes: Moving from Ultrafiltration toward Nanofiltration. *Macromolecules* **48**, 6153-6159 (2015).
18. M. Kumar, J. E. O. Habel, Y.-x. Shen, W. P. Meier, T. Walz, High-Density Reconstitution of Functional Water Channels into Vesicular and Planar Block Copolymer Membranes. *J. Am. Chem. Soc.* **134**, 18631-18637 (2012).
19. M. S. Mauter, M. Elimelech, C. O. Osuji, Stable Sequestration of Single-Walled Carbon Nanotubes in Self-Assembled Aqueous Nanopores. *J. Am. Chem. Soc.* **134**, 3950-3953 (2012).

20. C. L. Gonzalez, C. W. M. Bastiaansen, J. Lub, J. Loos, K. Lu, H. J. Wondergem, D. J. Broer, Nanoporous Membranes of Hydrogen‐bridged Smectic Networks with Nanometer Transverse Pore Dimensions. *Adv. Mater.* **20**, 1246-1252 (2008).
21. X. Feng, S. Nejati, M. G. Cowan, M. E. Tousley, B. R. Wiesenauer, R. D. Noble, M. Elimelech, D. L. Gin, C. O. Osuji, Thin Polymer Films with Continuous Vertically Aligned 1 nm Pores Fabricated by Soft Confinement. *ACS Nano* **10**, 150-158 (2016).
22. M. Yoshio, T. Kagata, K. Hoshino, T. Mukai, H. Ohno, T. Kato, One-Dimensional Ion-Conductive Polymer Films: Alignment and Fixation of Ionic Channels Formed by Self-Organization of Polymerizable Columnar Liquid Crystals. *J. Am. Chem. Soc.* **128**, 5570-5577 (2006).
23. X. Feng, M. E. Tousley, M. G. Cowan, B. R. Wiesenauer, S. Nejati, Y. Choo, R. D. Noble, M. Elimelech, D. L. Gin, C. O. Osuji, Scalable Fabrication of Polymer Membranes with Vertically Aligned 1 nm Pores by Magnetic Field Directed Self-Assembly. *ACS Nano* **8**, 11977-11986 (2014).
24. P. W. Majewski, M. Gopinadhan, W.-S. Jang, J. L. Lutkenhaus, C. O. Osuji, Anisotropic Ionic Conductivity in Block Copolymer Membranes by Magnetic Field Alignment. *J. Am. Chem. Soc.* **132**, 17516-17522 (2010).
25. M. Zhou, P. R. Nemade, X. Lu, X. Zeng, E. S. Hatakeyama, R. D. Noble, D. L. Gin, New Type of Membrane Material for Water Desalination Based on a Cross-Linked Bicontinuous Cubic Lyotropic Liquid Crystal Assembly. *J. Am. Chem. Soc.* **129**, 9574-9575 (2007).
26. M. Henmi, K. Nakatsuji, T. Ichikawa, H. Tomioka, T. Sakamoto, M. Yoshio, T. Kato, Self‐Organized Liquid‐Crystalline Nanostructured Membranes for Water Treatment: Selective Permeation of Ions. *Adv. Mater.* **24**, 2238-2241 (2012).
27. B. R. Wiesenauer, D. L. Gin, Nanoporous polymer materials based on self-organized, bicontinuous cubic lyotropic liquid crystal assemblies and their applications. *Polym. J.* **44**, 461 (2012).
28. E. W. Cochran, C. J. Garcia-Cervera, G. H. Fredrickson, Stability of the Gyroid Phase in Diblock Copolymers at Strong Segregation. *Macromolecules* **39**, 2449-2451 (2006).
29. G. P. Sorenson, K. L. Coppage, M. K. Mahanthappa, Unusually Stable Aqueous Lyotropic Gyroid Phases from Gemini Dicarboxylate Surfactants. *J. Am. Chem. Soc.* **133**, 14928-14931 (2011).
30. T. Sakamoto, T. Ogawa, H. Nada, K. Nakatsuji, M. Mitani, B. Soberats, K. Kawata, M. Yoshio, H. Tomioka, T. Sasaki, M. Kimura, M. Henmi, T. Kato, Development of Nanostructured Water Treatment Membranes Based on Thermotropic Liquid Crystals: Molecular Design of Sub‐Nanoporous Materials. *Adv. Sci.* **5**, 1700405 (2018).
31. M. A. Shannon, P. W. Bohn, M. Elimelech, J. G. Georgiadis, B. J. Mariñas, A. M. Mayes, Science and technology for water purification in the coming decades. *Nature* **452**, 301 (2008).
32. B. D. McCloskey, H. B. Park, H. Ju, B. W. Rowe, D. J. Miller, B. D. Freeman, A bioinspired fouling-resistant surface modification for water purification membranes. *J. Membr. Sci.* **413-414**, 82-90 (2012).
33. M. A. DePierro, C. A. Guymon, Polymer Structure Development in Lyotropic Liquid Crystalline Solutions. *Macromolecules* **47**, 5728-5738 (2014).
34. K. Nagai, Y. Ohishi, H. Inaba, S. Kudo, Polymerization of surface-active monomers. I. Micellization and polymerization of higher alkyl salts of dimethylaminoethyl methacrylate. *Journal of Polymer Science: Polymer Chemistry Edition* **23**, 1221-1230 (1985).
35. J. F. Hulvat, S. I. Stupp, Liquid-Crystal Templating of Conducting Polymers. *Angew. Chem. Int. Ed.* **42**, 778-781 (2003).
36. L. Sievens-Figueroa, C. A. Guymon, Cross-Linking of Reactive Lyotropic Liquid Crystals for Nanostructure Retention. *Chem. Mater.* **21**, 1060-1068 (2009).

37. B. A. Pindzola, B. P. Hoag, D. L. Gin, Polymerization of a Phosphonium Diene Amphiphile in the Regular Hexagonal Phase with Retention of Mesostructure. *J. Am. Chem. Soc.* **123**, 4617-4618 (2001).
38. M. E. Tousley, X. Feng, M. Elimelech, C. O. Osuji, Aligned nanostructured polymers by magnetic-field-directed self-assembly of a polymerizable lyotropic mesophase. *ACS Appl. Mater. Interfaces* **6**, 19710-19717 (2014).
39. M. C. Jennings, K. P. C. Minbiole, W. M. Wuest, Quaternary Ammonium Compounds: An Antimicrobial Mainstay and Platform for Innovation to Address Bacterial Resistance. *ACS Infect Dis.* **1**, 288-303 (2015).
40. Y. Jiao, L.-n. Niu, S. Ma, J. Li, F. R. Tay, J.-h. Chen, Quaternary ammonium-based biomedical materials: State-of-the-art, toxicological aspects and antimicrobial resistance. *Prog. Poly, Sci.* **71**, 53-90 (2017).
41. X. Lu, X. Feng, J. R. Werber, C. Chu, I. Zucker, J. H. Kim, C. O. Osuji, M. Elimelech, Enhanced antibacterial activity through the controlled alignment of graphene oxide nanosheets. *Proc. Natl. Acad. Sci. USA* **114**, E9793-E9801 (2017).
42. X. Lu, X. Feng, X. Zhang, M. N. Chukwu, C. O. Osuji, M. Elimelech, Fabrication of a Desalination Membrane with Enhanced Microbial Resistance through Vertical Alignment of Graphene Oxide. *Environ. Sci. Technol. Lett.*, DOI: 10.1021/acs.estlett.1028b00364 (2018).

Acknowledgements

This work was supported by NSF through PFI:AIR-TT IIP-1640375 and CBET-1703494. Facilities use was supported by the NSF MRSEC program (DMR-1119826) and the Yale Institute for Nanoscience and Quantum Engineering (YINQE). C.O.O. acknowledges additional financial support from NSF (DMR-1410568). K.K. acknowledges support from a JSPS Fellowship.

Author contributions

X.F. and C.O.O. conceived the ideas and designed the research. X.F. conducted the synthesis of the surfactant. X.F., L.S. and G.K. performed the structural characterization of the mesophase. X.F., Q.I, and Y.Z. fabricated the membranes and tested the filtration performances. X. L. conducted the CFU assays. All authors contributed to data analysis. X.F., Q.I, Y.Z., and C.O.O. co-wrote the manuscript.

Competing interests

The authors declared that they have no competing interests.

Data and materials availability

All data needed to evaluate the conclusions in the paper are present in the paper and/or the Supplementary Materials. Additional data related to this paper may be requested from the authors.

Supplementary materials

Figure S1. METDAB/water binary phase diagram as determined by POM and X-ray scattering.

Figure S2. Polymerization of H_1 mesophases formed by METDAB/water binary systems in the absence of cross-linkers.

Figure S3. Structural characterization of an H_1 mesophase containing only one cross-linking species in the hydrophobic core of cylindrical micelles before and after UV-initiated cross-linking.

Figure S4. X-ray scattering and POM data showing slight structural changes in the H_1 gel, the crosslinked H_1 mesophase and the swelled polymer.

Figure S5. Schematic illustration for the preparation of TEM samples.

Figure S6. Schematic illustration of the pore dimensions.

Figure S7. SEM images showing the cross-sections of the H_1/PAN composite membranes.

Figure S8. Photos showing the stirred cell used for the nanofiltration test.

Figure S9. The time-dependent solute rejection for H_1 composites and the static solute adsorption experiment for free-standing H_1 membranes.

Figure S10. UV-Vis spectrum and photographs demonstrating the competitive solute separation of CV and VB2.

Section S1. Calculation of the pore dimensions in an H_1 membrane.

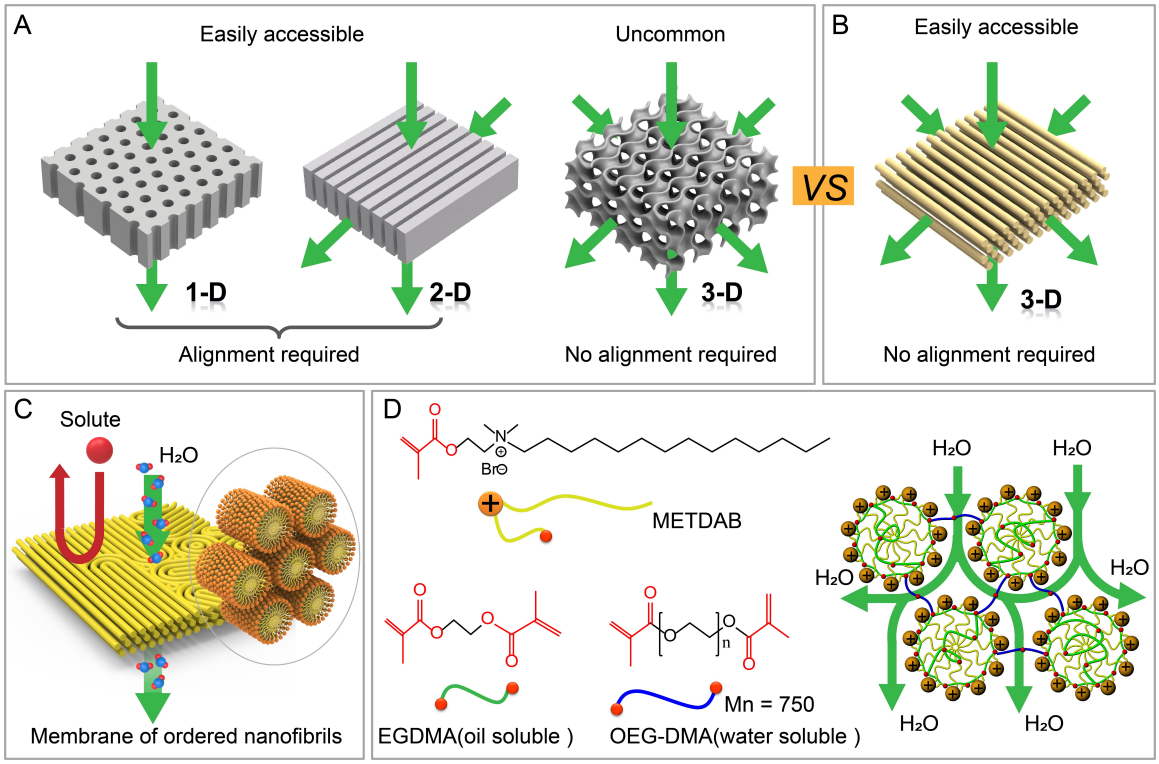

Figure 1

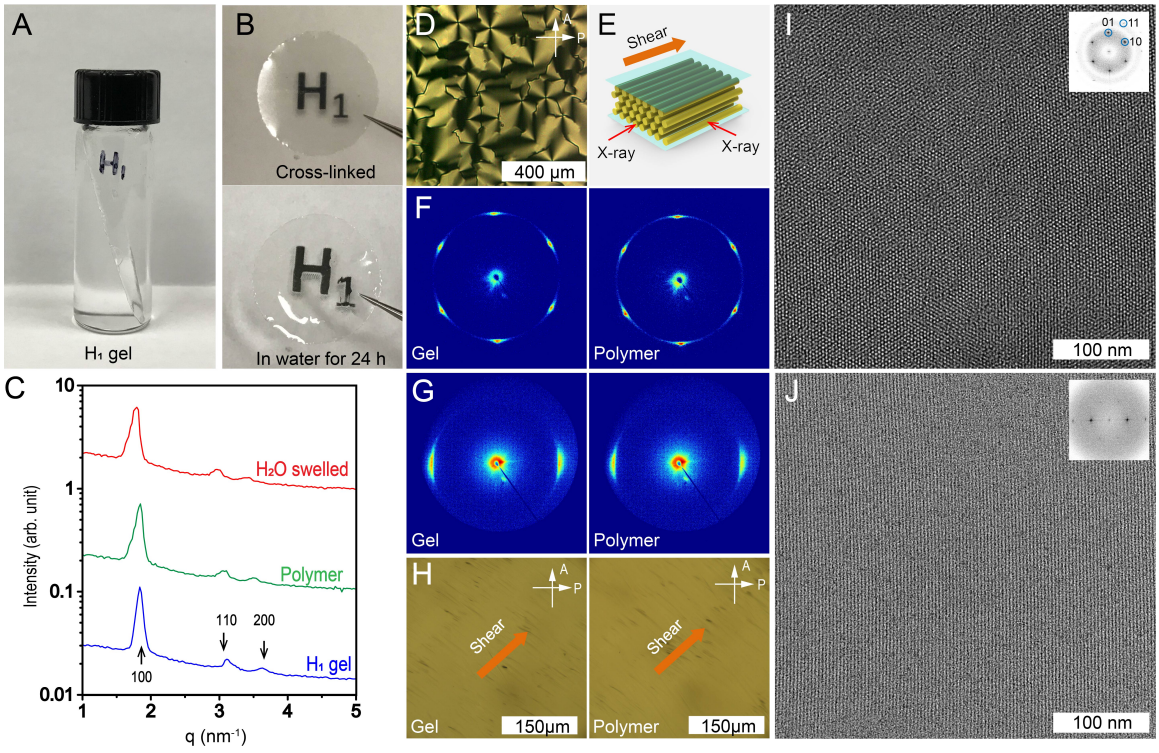

Figure 2

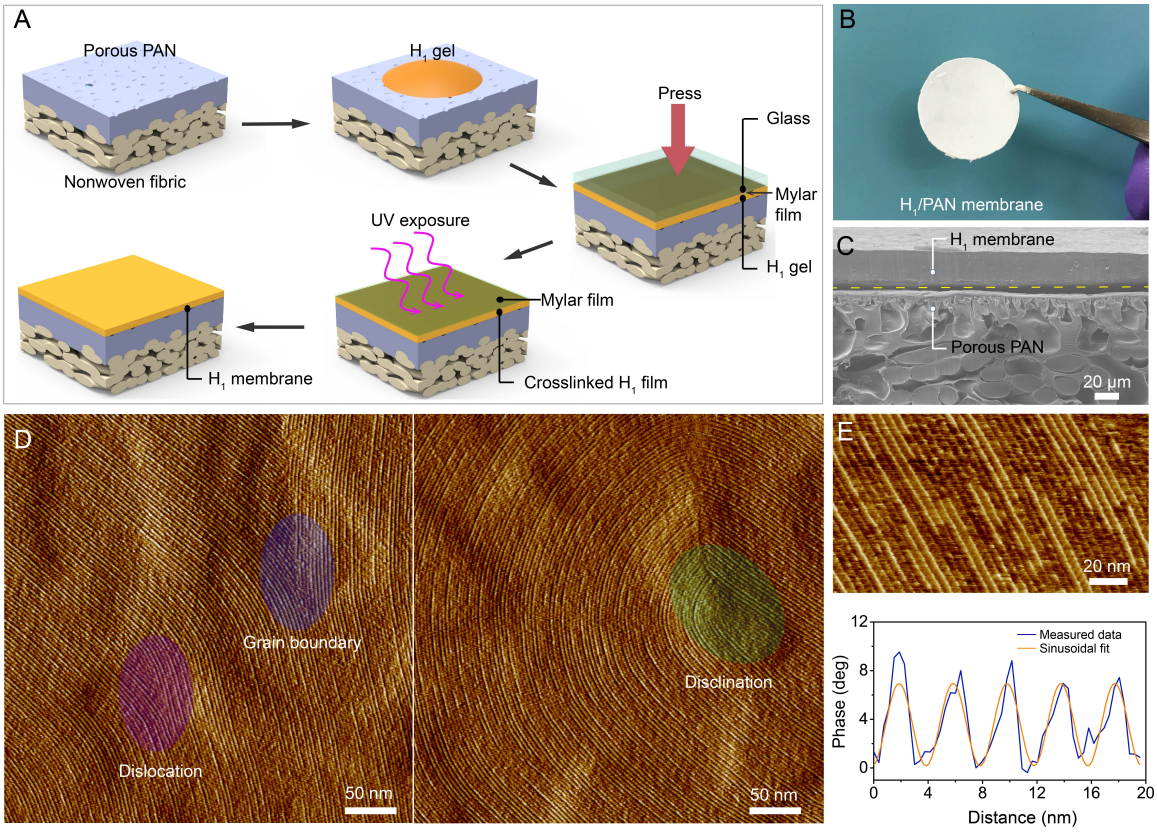
A
Porous PAN
Nonwoven fibric
H1 gel
Press
Glass
Mylar film
H1 gel
UV exposure
Mylar film
Crosslinked H1 film
H1 membrane
B
H1/PAN membrane
C
H1 membrane
Porous PAN
20 μm
D
Grain boundary
Dislocation
50 nm
Disclination
50 nm
E
20 nm
Measured data
Sinusoidal fit
Phase (deg)
Distance (nm)

Figure 3

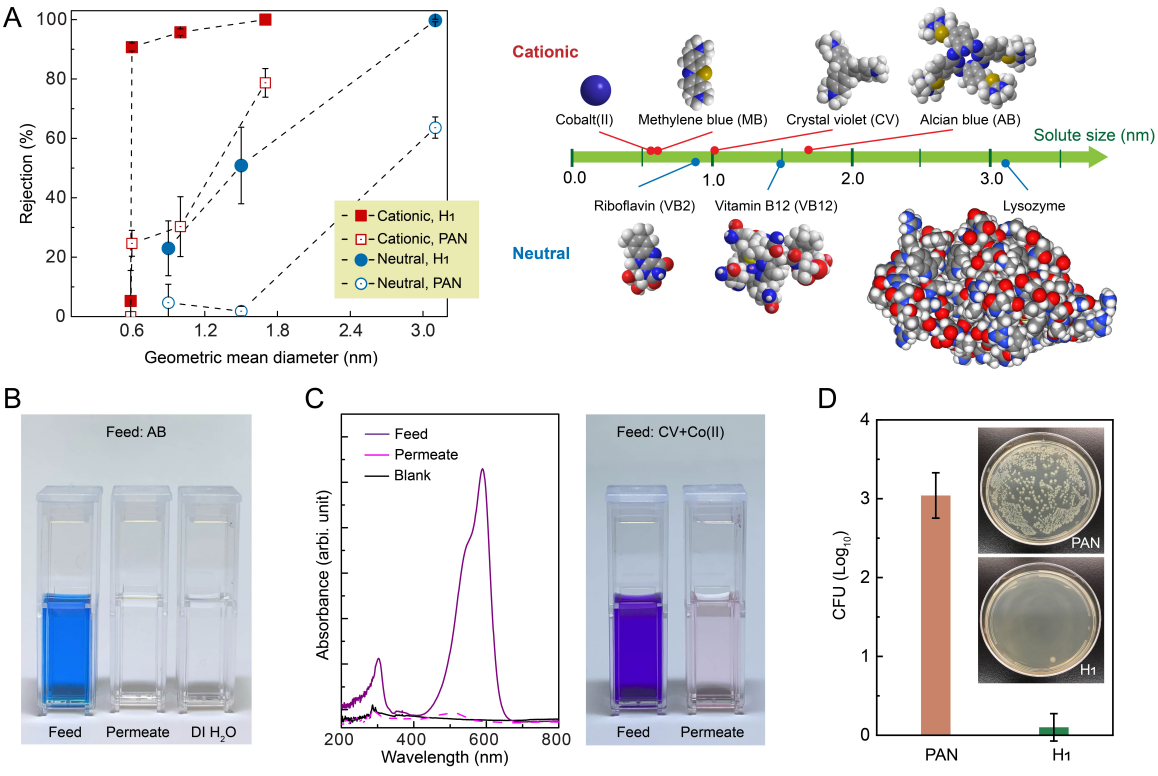
A
Rejection (%)
Geometric mean diameter (nm)
Cationic, H1
Cationic, PAN
Neutral, H1
Neutral, PAN
Cationic
Cobalt(II)
Methylene blue (MB)
Crystal violet (CV)
Alcian blue (AB)
Solute size (nm)
Riboflavin (VB2)
Vitamin B12 (VB12)
Lysozyme
Neutral
B
Feed: AB
Feed
Permeate
DI H2O
C
Feed
Permeate
Blank
Absorbance (arbi. unit)
Wavelength (nm)
Feed: CV+Co(II)
Feed
Permeate
D
CFU (Log10)
PAN
H1
PAN
H1

Figure 4

Supplementary Materials

Precise nanofiltration in a fouling-resistant self-assembled membrane with water-continuous transport pathways

Xunda Feng[1,2,†], Qaboos Imran[2,3,†], Yizhou Zhang[3,†], Lucas Sixdenier [4], Xinglin Lu[2], Gilad Kaufman[2], Uri Gabinet[2,3], Kohsuke Kawabata[5], Menachem Elimelech[2], and Chinedum O. Osuji[2,3*]

[1] Center for Advanced Low-dimension Materials, State Key Laboratory for Modification of Chemical Fibers and Polymer Materials, Donghua University, Shanghai 201620, China

[2] Department of Chemical and Environmental Engineering, Yale University, New Haven, CT 06511, USA

[3] Department of Chemical and Biomolecular Engineering, University of Pennsylvania, Philadelphia PA 19104

[4] ESPCI Paris, 10 Rue Vauquelin, 75005 Paris, France

[5] Department of Chemistry, Graduate School of Science, Tohoku University, 6-3 Aoba, Aramaki, Aoba-Ku, Sendai, Japan

*Email: cosuji@seas.upenn.edu

† These authors contribute equally.

The PDF file includes:

Figure S1. METDAB/water binary phase diagram as determined by POM and X-ray scattering.

Figure S2. Polymerization of H_1 mesophases formed by METDAB/water binary systems in the absence of cross-linkers.

Figure S3. Structural characterization of an H_1 mesophase containing only one cross-linking species in the hydrophobic core of cylindrical micelles before and after UV-initiated cross-linking.

Figure S4. X-ray scattering and POM data showing slight structural changes in the H_1 gel, the crosslinked H_1 mesophase and the swelled polymer.

Figure S5. Schematic illustration for the preparation of TEM samples.

Figure S6. Schematic illustration of the pore dimensions.

Figure S7. SEM images showing the cross-sections of the H_1/PAN composite membranes.

Figure S8. Photos showing the stirred cell used for the nanofiltration test.

Figure S9. The time-dependent solute rejection for H_1 composites and the static solute adsorption experiment for free-standing H_1 membranes.

Figure S10. UV-Vis spectrum and photographs demonstrating the competitive solute separation of CV and VB2.

Section S1. Calculation of the pore dimensions in an H_1 membrane.

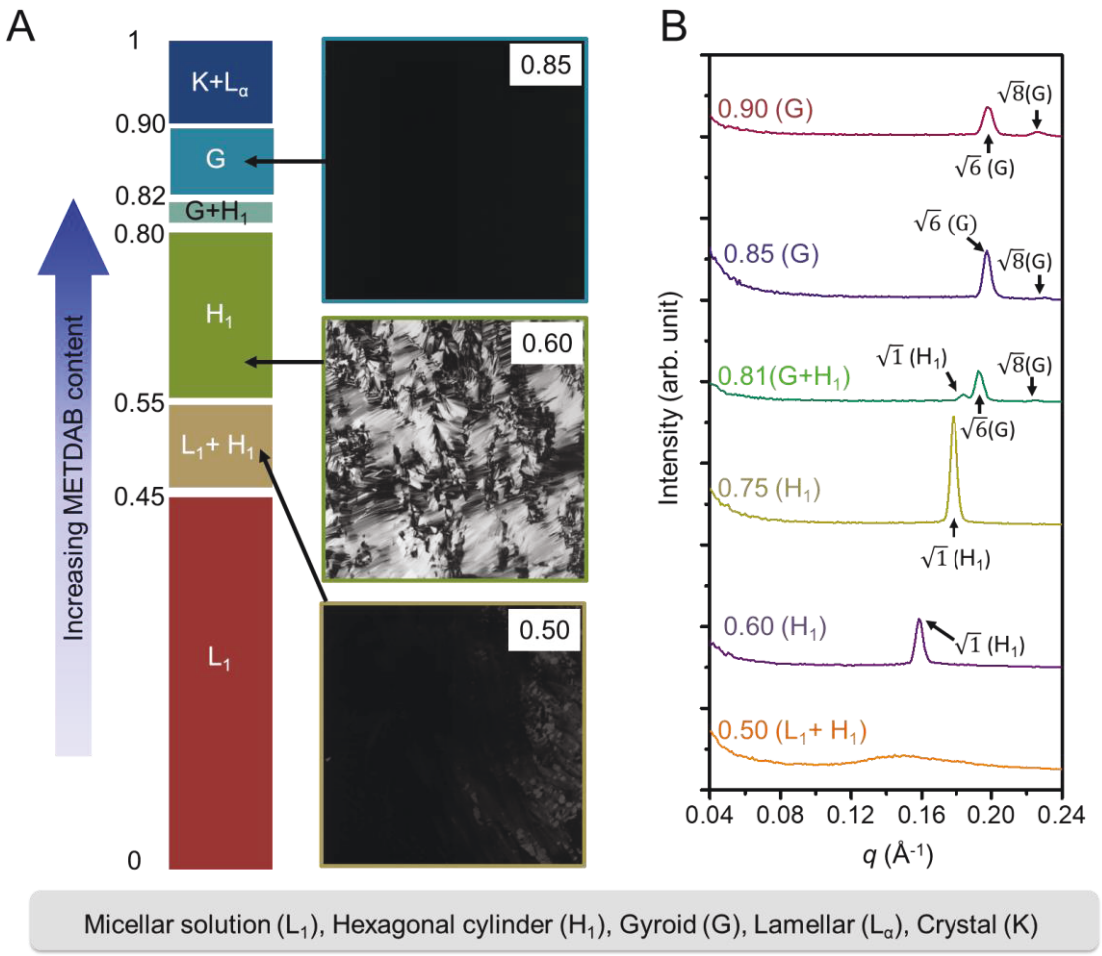

Figure S1. METDAB/water binary phase diagram as determined by POM and X-ray scattering. The weight concentrations of METDAB are shown in the phase diagram. As the concentration of METDAB was increased, the surfactant/water mixtures followed a phase sequence of micellar solution (L_1), hexagonal cylinder (H_1), gyroid (G), lamellar (L_α), and crystal (K). Selective (A) POM images and (B) X-ray scattering data represent this sequence.

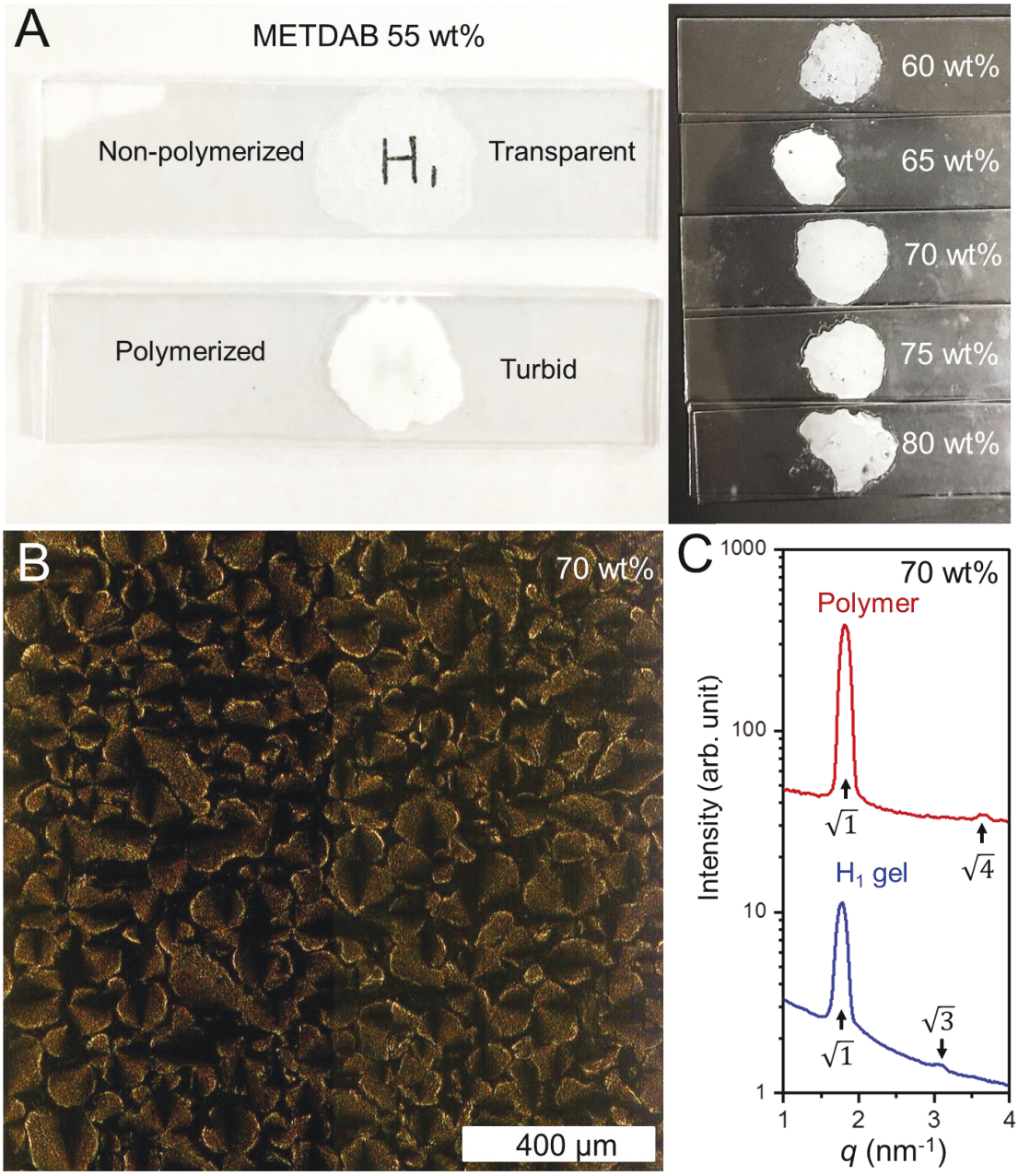

Figure S2. Polymerization of H_1 mesophases formed by METDAB/water binary systems in the absence of cross-linkers. (A) Photos showing remarkable cloudiness in polymerized H_1 samples with different METDAB contents ranging from 55 to 80 wt%. (B) POM image of the polymerized H_1 mesophase with 70 wt% METDAB shows loss of the typical LC texture. (C) 1-D SAXS data displays that the ratio of peak locations changes from 1: √ 3 to 1: √ 4 after polymerization, indicative of disruption of the H_1 morphology. Photo credit: Xunda Feng, Yale University.

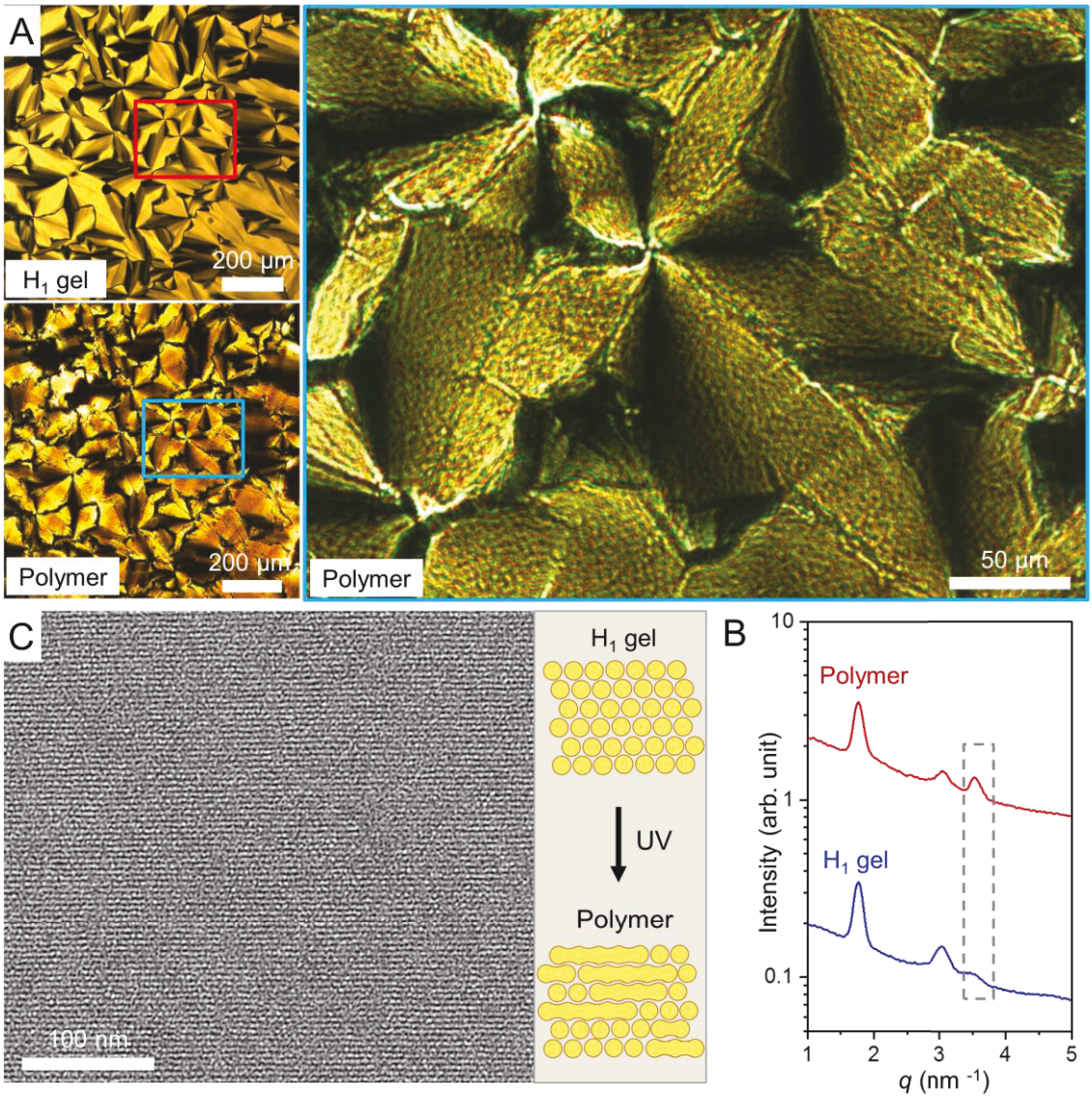

Figure S3. Structural characterization of an H_1 mesophase containing only one cross-linking species in the hydrophobic core of cylindrical micelles before and after UV-initiated cross-linking. The cross-linker is 1,6-hexanediol dimethacrylate (HDMA). The mesophase contained 70 wt% METDAB, 6 wt% HDMA, and 24 wt% water. (A) Characteristic developable domain texture of the H_1 mesophase observed using POM before crosslinking. After UV induced cross-linking, a superficially similar, but discernably different, birefringent texture was observable in low magnification POM images. A magnified view (right) more clearly shows the emergence of optical inhomogeneities within the developable domains, reflecting disruption of the original H_1 morphology. Rectangles highlight the change of the LC texture induced polymerization. (B) X-ray scattering data showing intact peak locations but an unexpected increase of the intensity of the (200) peak after UV-induced cross-linking. (C) TEM image and schematic, illustrate the tendency of the hexagonal cylinders to transform to lamellar structures after cross-linking.

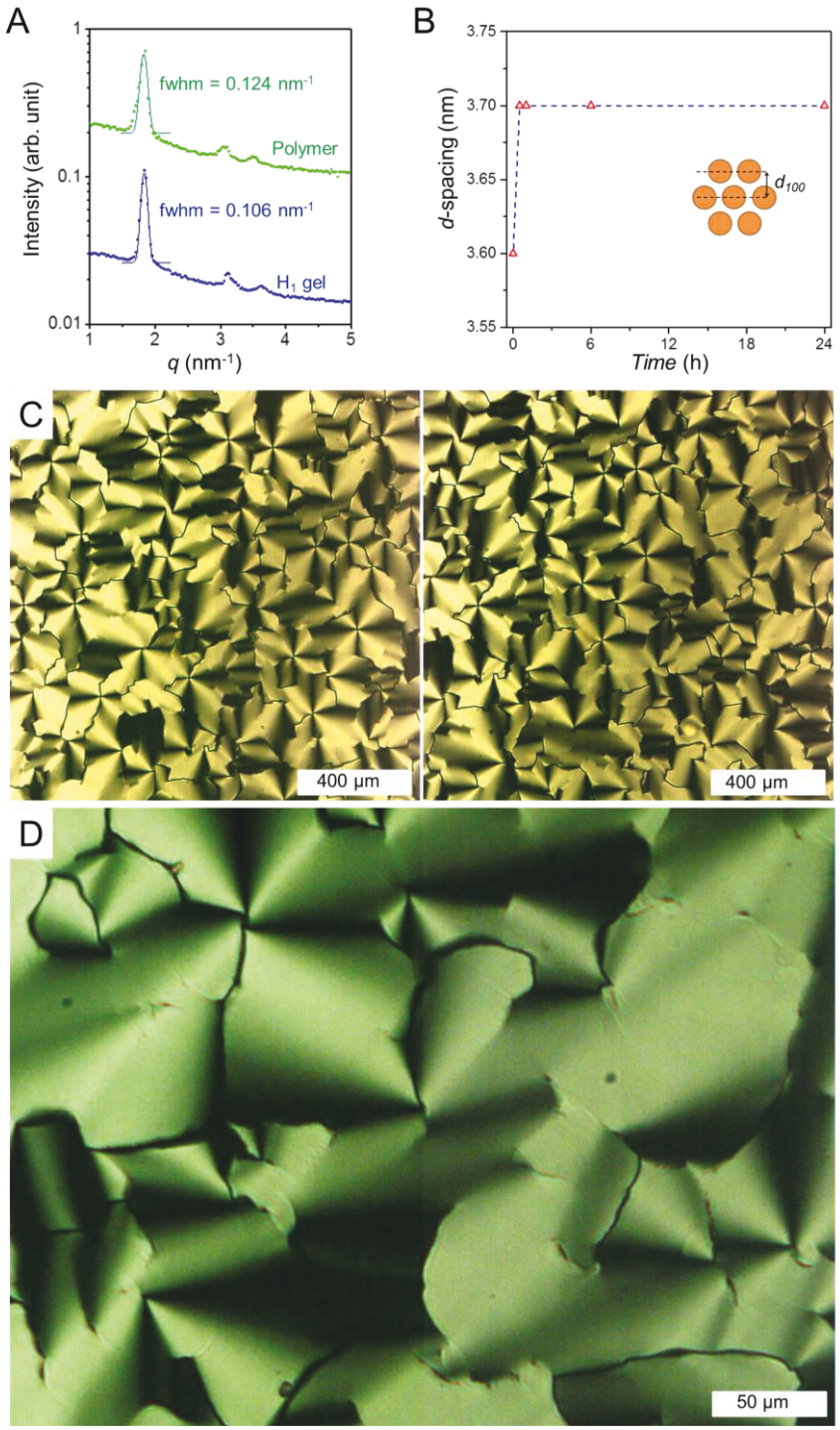

Figure S4. X-ray scattering and POM data showing slight structural changes in the H_1 gel, the crosslinked H_1 mesophase and the swelled polymer. (A) Gaussian fits of the (100) SAXS peaks of the H_1 gel and the corresponding polymer to obtain the values of full width at half maximum (fwhm). (B) Time dependent d_{100} spacing of the cross-linked H_1 membrane immersed in water as determined by X-ray scattering. (C) Low-magnification and (D) High-magnification POM images of the crosslinked H_1 mesophase.

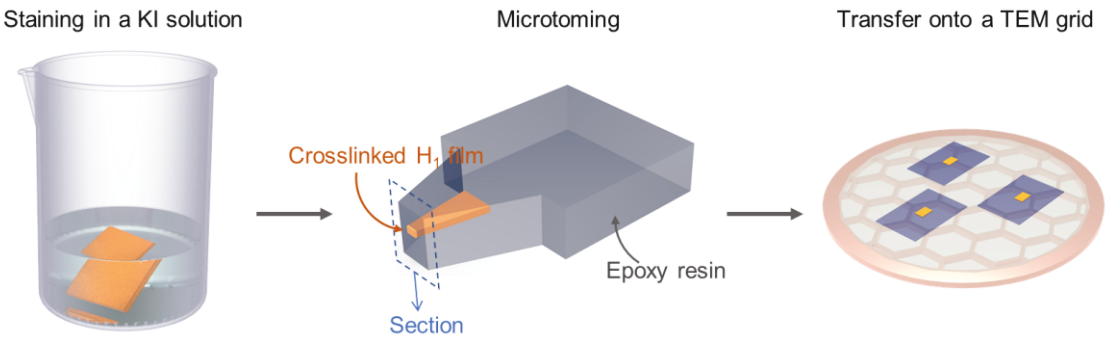

Figure S5. Schematic illustration for the preparation of TEM samples.

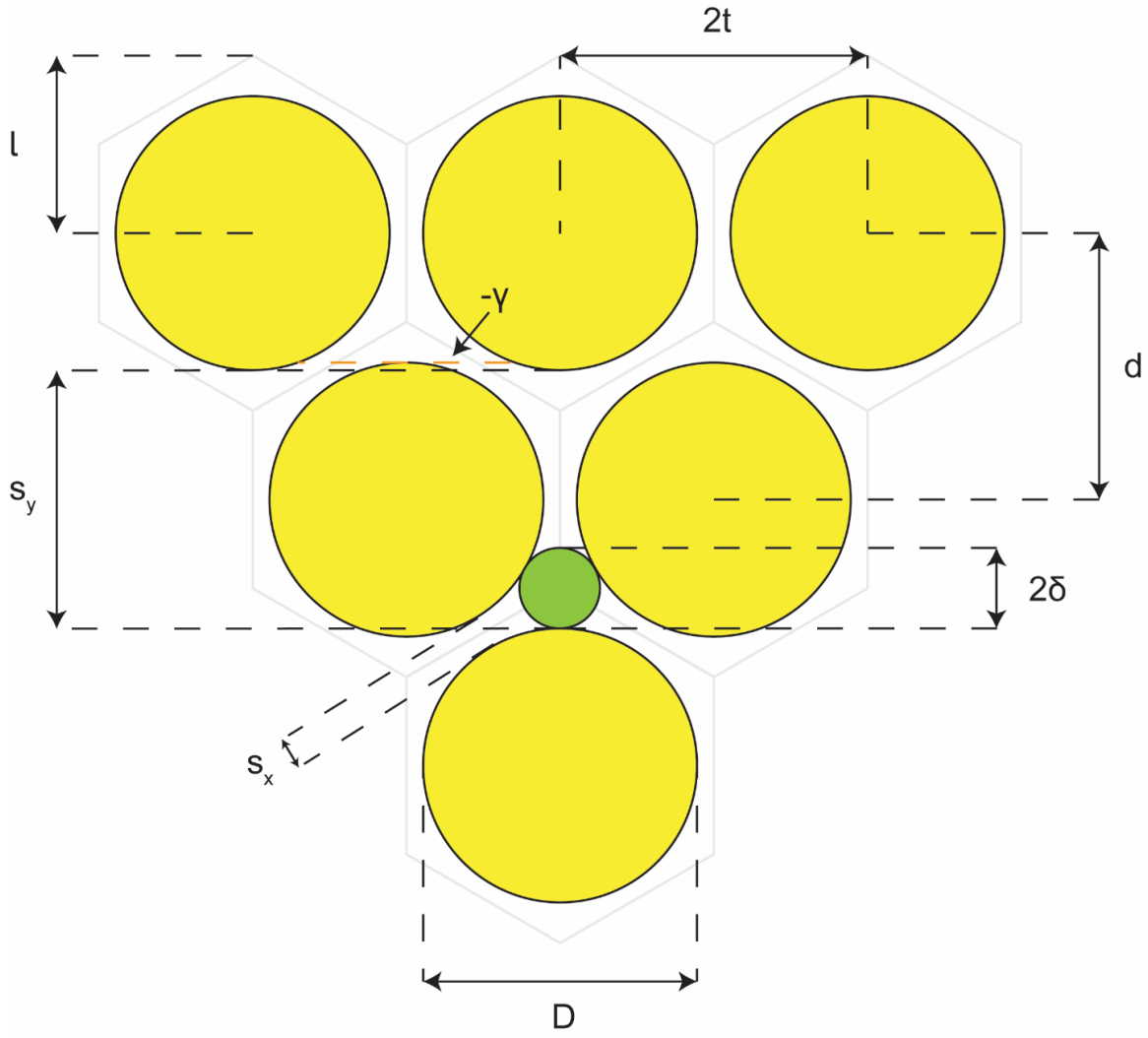

Figure S6. Schematic illustration of the pore dimensions. The controlling dimensions of the structure are ~ 1.1 nm (2 δ) for transport in parallel and ~ 0.5 nm (S_x) for transport in perpendicular. Calculations are detailed in Section S1.

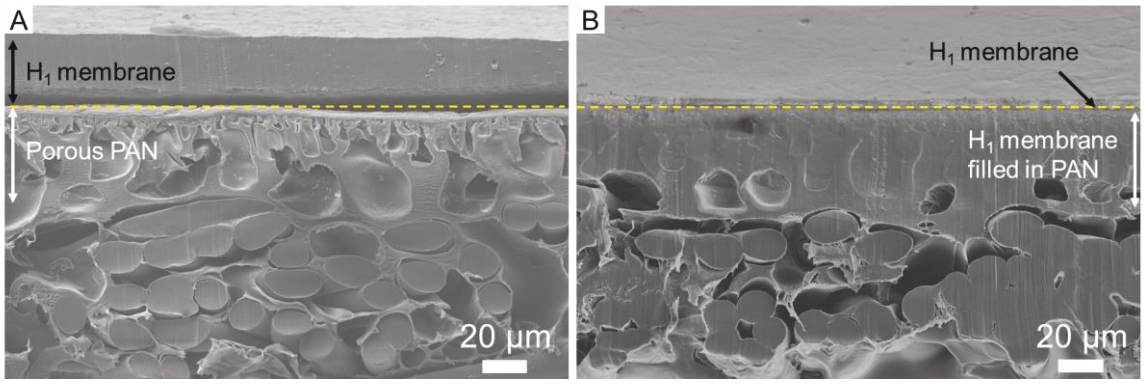

Figure S7. **SEM images showing the cross-sections of the H_1/PAN composite membranes**. The H_1 gel infiltrates the pores of the PAN support membrane during the pressing stage and the infiltrated H_1 is eventually crosslinked along with the surface H_1 layer.

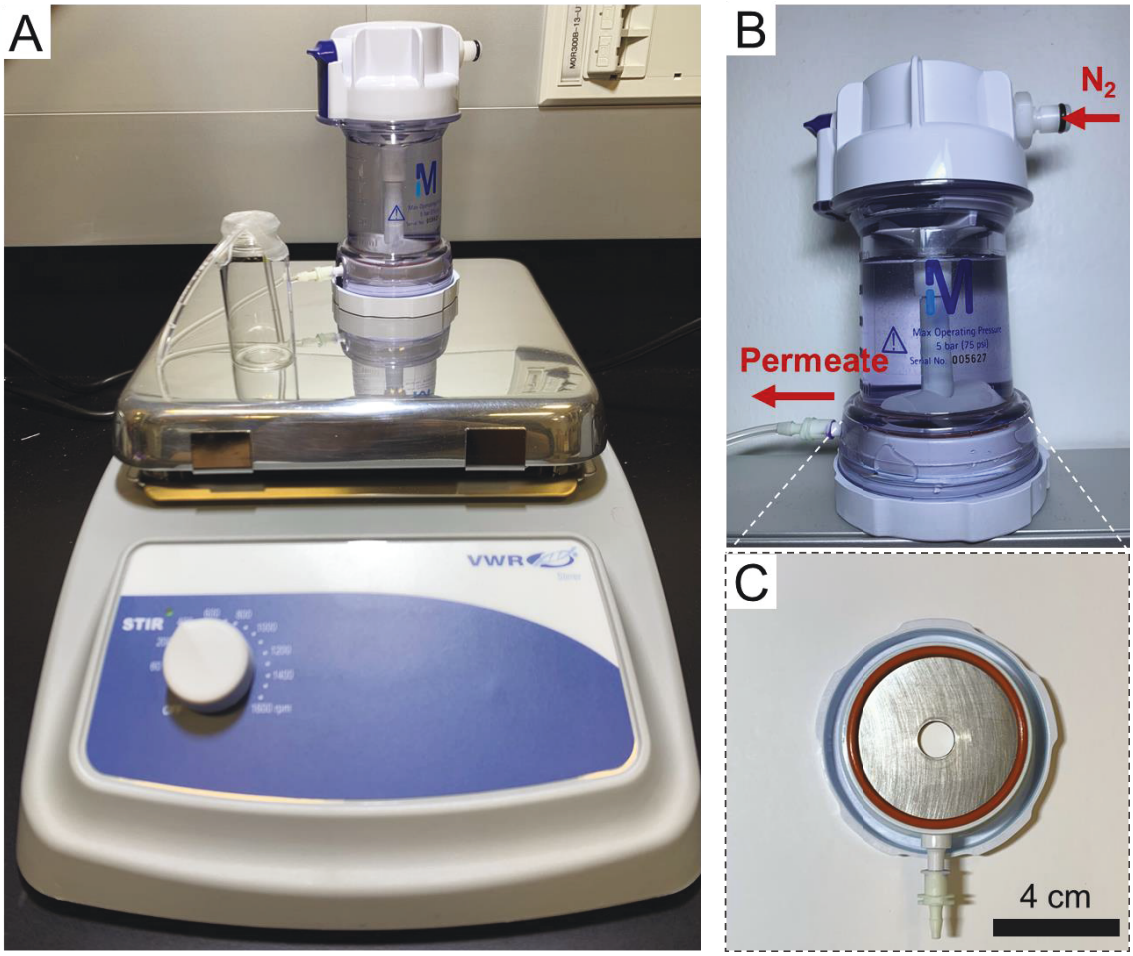

Figure S8. Photos showing the stirred cell used for the nanofiltration test. (A) 50 mL EMD Millipore Amicon (UFSC05001) stirred cell. A stirring speed of 400 rpm was employed. (B) Photo showing the inlet of the compressed N_2 and the outlet of the permeate. (C) The active testing area of the membrane coupon was a circular area with a diameter of 1.1 cm. Photo credit: Yizhou Zhang, University of Pennsylvania.

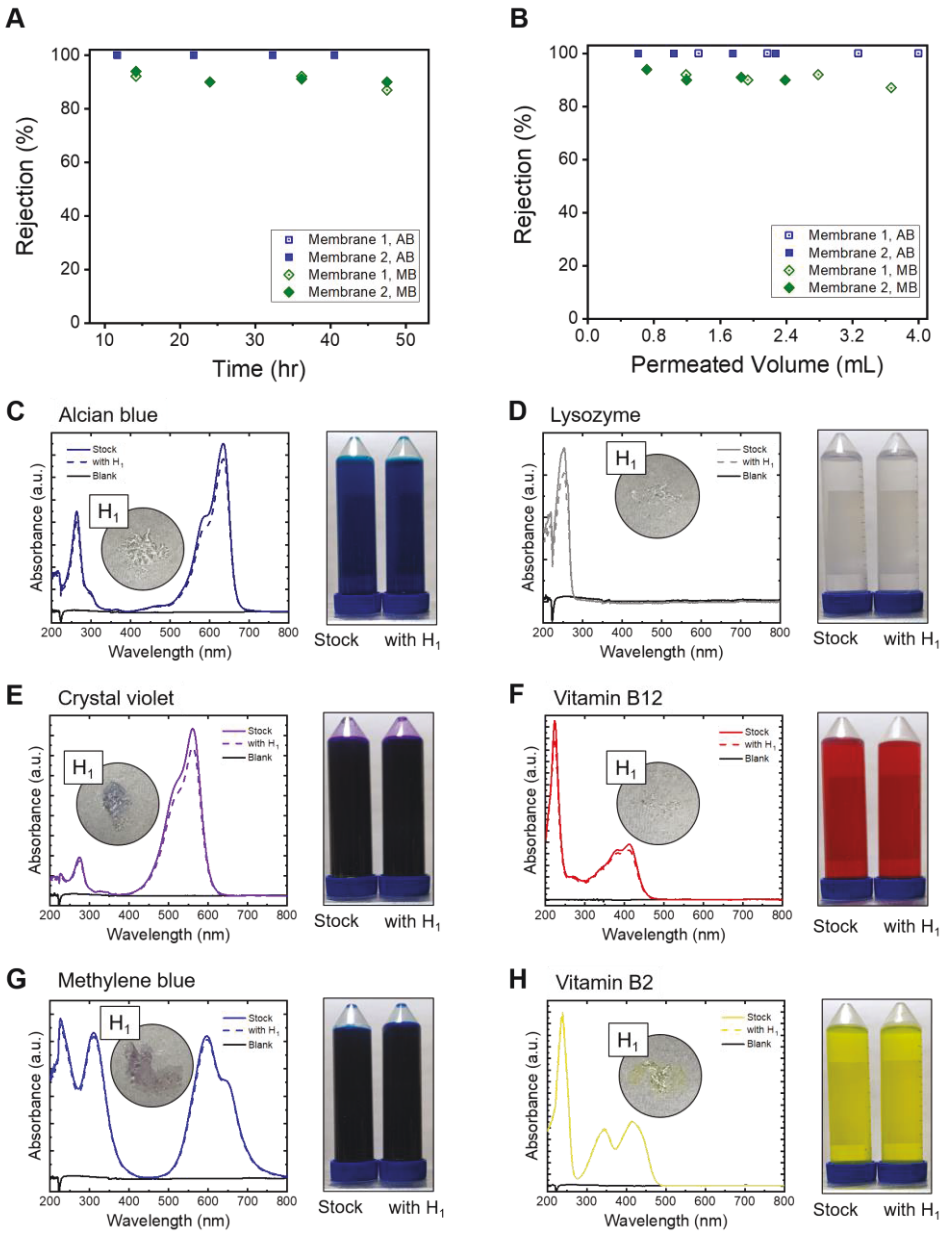

Figure S9. The time-dependent solute rejection for H_1 composites and the static solute adsorption experiment for free-standing H_1 membranes. The time-dependent solute rejection tests suggest the separation performance of H_1 composite is independent of (A) experiment time and (B) permeated solution volume. UV-Vis spectroscopy was employed to determine the possible adsorption of dye molecules by the membranes. Dyes tested were (C) Alcian blue, (D) lysozyme, (E) crystal violet, (F) vitamin B_{12}, (G) methylene blue and (H) vitamin B_2. The experiment was performed with a same initial solute concentration as utilized during single solute rejection experiment, with a packing ratio of ~0.2 g membrane per L solution. The membranes did not uptake a significant amount of solute during prolonged soaking, suggesting adsorption did not affect the results in single solute rejection experiments. Photo credit: Yizhou Zhang, University of Pennsylvania.

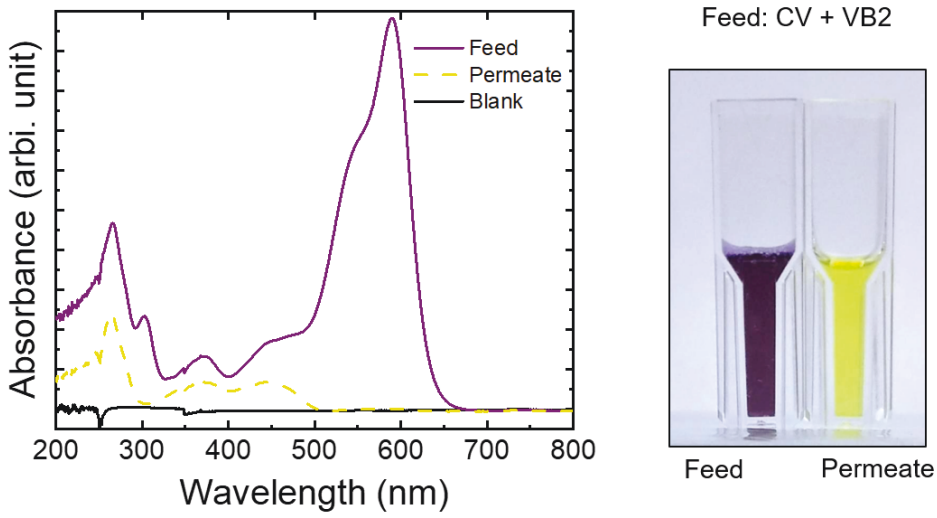

Figure S10. **UV-Vis spectrum and photographs demonstrating the competitive solute separation of CV and VB2.** The membrane selectively rejects CV while allowing VB2 to partially permeate through (R ~ 50%). Photo credit: Yizhou Zhang, University of Pennsylvania.

Section S1. Calculation of the pore dimensions in an H_1 membrane.

As simply illustrated in Figure S6, the geometry of an H_1 membrane consists of a continuous water transport path and discontinuous cylinders (colored in yellow). The volume fractions of the cylinders ϕ and the water transport path 1-ϕ are assumed to be 0.72 and 0.28, respectively, on the basis of the original composition of the H_1 gel. The distance of the neighboring (100) planes d was determined by X-ray scattering to be 3.6 nm.

$$l = \frac{2d}{3}$$

$$\delta = l - \frac{D}{2}$$

$$\mathrm{t} = \sin(\frac{\pi}{3})l$$

$$2\delta = \mathrm{d}\left[\frac{4}{3} - \left(\frac{8\phi}{\sqrt{3}\pi}\right)^{\frac{1}{2}}\right] = 1.09\ \mathrm{nm}$$

$$S_x = 2t - D = \mathrm{d}\left[\sqrt{\frac{4}{3}} - \left(\frac{8\phi}{\sqrt{3}\pi}\right)^{\frac{1}{2}}\right] = 0.45\ \mathrm{nm}$$

$$S_y = 3l - D = \mathrm{d}\left[2 - \left(\frac{8\phi}{\sqrt{3}\pi}\right)^{\frac{1}{2}}\right] = 3.5\ \mathrm{nm}$$

$$\gamma = \frac{3l}{2} - D = \mathrm{d}\left[1 - \left(\frac{8\phi}{\sqrt{3}\pi}\right)^{\frac{1}{2}}\right] = -0.10\ nm$$